

NMR measurements of hyperpolarized ^3He gas diffusion in high porosity silica aerogels

Geneviève Tastevin* and Pierre-Jean Nacher†

Laboratoire Kastler Brossel, 24 rue Lhomond, 75231 Paris Cedex 05, France‡

(Dated: October 19, 2018)

Hyperpolarized ^3He is used to nondestructively probe by NMR the structure of custom-made and commercial silica aerogels (97% and 98.5% porous). Large spin-echo signals are obtained at room temperature and very low magnetic field (2 mT) even with small amounts of gas. Attenuation induced by applied field gradients results from the combined effects of gas diffusion and confinement by the porous medium on atomic motion. Nitrogen is used as a buffer gas to reach equivalent ^3He pressures ranging from 5 mbars to 3.5 bars. The observed pressure dependence suggests a non-uniform structure of the aerogels on length scales up to tens of micrometers. A description by broad phenomenological distributions of mean free paths is proposed, and quantitatively discussed by comparison to numerical calculations. The investigated aerogel samples exhibit different effective diffusion characteristics despite comparable nominal porosities.

Keywords: Silica aerogel; spin diffusion; hyperpolarized helium; low field NMR.

Article published in the Journal of Chemical Physics.
Reference : J. Chem. Phys. **123**, 064506 (2005)

I. INTRODUCTION

Silica aerogels are highly porous solids obtained by sol-gel process [1]. Their very open structure consists of a delicate, highly ramified backbone network of randomly interconnected thin silica strands, formed by aggregation of small silica clusters [2, 3]. Mechanically robust, they exhibit very low densities, thermal conductivities, dielectric constants and sound velocities, as well as poor chemical reactivity and large specific areas. Despite high synthesizing costs and difficulties, they have been commercially produced for civil and military use and they have found applications in thermal insulation, manufacture of materials and coatings, catalysis, gas storage and filtering, Cerenkov radiation detection, etc. In science, their unique properties make them attractive for cutting-edge studies in optics, acoustics, chemical physics, low-temperature physics, nuclear physics, space investigations, laser tests, microelectronics, electrical engineering, life sciences and bioengineering [1, 4, 5]. The density and microstructure of the aerogels can be precisely controlled by adjusting the growth chemistry [4, 6–8]. This makes them particularly suited for a variety of investigations on bulk, film or layer systems in weakly confined random geometries.

Considerable effort has been devoted to the study of phase transitions in aerogel [9–12], in particular with helium at low temperature to probe statistical and quantum

effects [10, 12, 13]. The silica network provides a structural disorder background to the fluid where it is imbedded, but occupies only a very small fraction of the sample volume. Recently, extremely high (up to 99.5%) porosity aerogels have been used to study impurity scattering effects on unconventional pairing states in superfluid ^3He [14, 15] and changes of critical exponents in superfluid ^4He [16]. Strong modifications of the phase diagram occur when the correlation length of the order parameter in the fluid becomes comparable to that of aerogel. The microstructure of the samples used in the experiments must hence be characterized at the appropriate length scales, that range from nanometers (15–80 nm in superfluid ^3He [17], 3–100 nm in superfluid ^4He [16, 18]) to tens of microns (mean free path, mfp, of unpaired ^3He quasiparticles at low pressure and temperature [12]).

In contrast with Vycor glass or porous gold, for instance, there is no single or dominant length scale to characterize the distribution of pores and silica in aerogel. Aerogel is known to be fractal at very small scales, a feature revealed both by small angle scattering (SAS) measurements with x rays or neutrons, and computer simulations of the growth process [2, 19, 20]. Self-similar structures range over correlation length scales from a few nanometers to hundreds of nanometers (depending on catalysis conditions and kinetics of the gelation process), above which the medium appears to be fairly homogeneous. Actual homogeneity at microscopic level, and relevance of a description solely based on the fractal dimension and one correlation length parameter, are key issues for the interpretation of all physical measurements [12], acutely debated in the case of superfluid ^3He and ^4He in aerogel [15, 21]. Discrepancies between experimental results are common and, most generally, tentatively attributed to unknown sample-to-sample microscopic variations (due to growth conditions, or insufficient characterization [12]). In addition, meso- or macroscopic inhomogeneities may develop during sample preparation, mounting, or use at low temperature (due to mechani-

*Electronic address: genevieve.tastevin@lkb.ens.fr

†Electronic address: pierre-jean.nacher@lkb.ens.fr

‡Research unit of the Ecole Normale Supérieure, and of the Pierre et Marie Curie University (Paris 6), associated to the Centre National de la Recherche Scientifique (UMR 8552).

cal or thermal stress [22]). Unfortunately, conventional techniques such as mercury intrusion porosimetry, thermoporometry, or nitrogen adsorption/desorption, are not suitable to characterize the aerogel pore structure accurately [23].

Nuclear magnetic resonance (NMR) is an established noninvasive technique to characterize porous media on a microscopic scale [24, 25]. Gas probes are of particular interest, because they can easily penetrate the porous matrix and exhibit fast diffusion rates that are conveniently varied over a wide range of values by pressure control. Compared to other inert species, ^3He may be considered as an ideal candidate probe for diffusion measurements: this spin-1/2 atom has long intrinsic relaxation times, and a resonance frequency fairly insensitive to most changes of its local environment [26, 27]. Suitable sensitivity is usually achieved using both high pressure and high magnetic field [27, 28] to compensate for the low density of the gas. With laser optical pumping techniques, high nuclear polarizations (hyperpolarizations) can be achieved independently of the magnetic field strength, and very high magnetization densities are obtained even at low pressures. Submillimetric imaging and diffusion measurements of hyperpolarized gases in free or confined spaces have been demonstrated both at high and low magnetic field [29–32], and used for various purposes including *in vivo* characterization of the lung alveolar airspaces for medical applications [33–36]. In the present work, we use hyperpolarized ^3He NMR to non-destructively probe the void spaces in high porosity silica aerogels identical to those used in most low-temperature experiments. With probe gas mfp's ranging from a fraction of micrometer to a few tens of micrometers when pressure is varied, this technique yields a unique type of information on the structure of these materials.

We had previously performed preliminary measurements on aerogel samples to test the feasibility of room temperature NMR investigations [37–39]. They suggested a non-uniform distribution of density of silica strands in this system, in contrast, for instance, with the single quasiparticle mfp value obtained by spin diffusion measurements in ^3He - ^4He dilute solutions [40]. We have now undertaken a more extended investigation to confirm this result, using an improved experimental setup. In this article, we report on a systematic study over a broader range of gas pressures that has been carried out to probe several samples of custom-made and commercially produced aerogels. Our former conclusions [38, 39] are confirmed. We show that all aerogels exhibit the same qualitative behavior, characterized by a pressure dependence of the gas diffusion coefficient that excludes a description of the aerogel by a single characteristic length. Significant differences are observed between the various samples, that do not correlate with the specified aerogel porosities and may rather be associated to differences in growth conditions. We also propose a phenomenological description of gas diffusion in aerogel based on broad power-law distributions of mfp's. Their main features are

quantitatively derived from the NMR data analysis, and discussed on the basis of computer calculations.

II. EXPERIMENT

A. Aerogel samples

Six samples of aerogel with 97% and 98.5% nominal porosities have been studied. One is custom made, and all others come from specialized manufacturers.

Sample M is a 98.5% open custom-made aerogel prepared by hydrolysis and polymerization of tetraethoxysilane, dilution in acetonitrile, gelation after addition of ammonia, and supercritical drying in an excess of solvent to preserve the delicate structure [41]. Because of the base catalyzing, the gelation process is believed to be diffusion-limited aggregation of small silica clusters (1–3 nm in diameter). This type of aerogel, used in many low-temperature experiments, has been fairly characterized at small length scales using experimental (scanning and transmission electron micrography, SEM and TEM; SAS of x rays and neutrons) and numerical (diffusion-limited cluster aggregation, DLCA, growth models) techniques [20]. The nanostructure of computer-generated aerogels, nicely reproducing that of real samples probed by SEM/TEM and SAS, can be most conveniently visualized (see, e.g., [12, 20] for 2D or 3D images) and statistically analyzed. On custom-made 98.5% samples similar to ours, SAS of x rays shows a fractal-like distribution of silica extending up to a length scale of 65–100 nm [13, 16], from which a purely geometrical mfp on the order of 270 nm can be calculated [42]. In a comparable DLCA model (98.2% porosity), the very dilute aerogel structure is found to be organized so that half of the widely open volume lies farther than 10 nm from some silica, while none of it is farther than 35 nm [42]. Recently, path-length distributions have been analyzed in simulated aerogels using randomly sampling straight-line trajectories [43], and finite-size hard spheres displacements to mimic experimental conditions [44]. The estimated ^3He quasiparticle mfp significantly exceeds in aerogel that of a randomly distributed medium of identical volume density (180 and 120 nm, respectively, for a 98.5% open sample [44]).

Aerogel M has been grown in a cylindrical glass container (inner diameter 12 mm, height 37 mm) partly filled with a set of three glass tubes (diameter 6×4 mm, height 30 mm, and axes parallel to that of the container). It has been produced as a transparent, crack-free sample attached to the glass walls. An epoxy end cap for the aerogel container is glued to allow leak-tight connection to the ^3He polarization system, with negligible dead volume between the free aerogel surface and the epoxy cap (Stycast 1266 A/B, Emerson and Cuming, Billerica, MA, USA).

Sample A is a 97% porous aerogel with nominal specific area 465 m²/g manufactured by Airglass, Staffanastrop,

Sweden. The cylindrical sample (diameter 12.5 mm, height 10.8 mm) is enclosed in a matching PMMA [45] container. The container and end cap are machined so that the aerogel gently fits in, avoiding mechanical stress (~ 0.05 mm gap size).

Samples J_1 – J_4 are four pieces of 97% porous aerogel with nominal specific area $510 \text{ m}^2/\text{g}$ manufactured by Matsushita Electric Works, Osaka, Japan. J_1 and J_2 originally had identical parallelepipedic shapes (sections $15 \times 15.5 \text{ mm}^2$, thicknesses 9.7 mm). J_1 , accidentally crushed before use, is reduced in thickness by 1.7–2.7 mm (from end to end along its longest dimension, with a noticeable transverse fracture line). J_3 and J_4 have cylindrical shapes (diameters 9.1 and 7.7 mm, lengths 10.7 and 10.5 mm, respectively). Their original rough ends have been cut flat using a silicon carbide disk driven at very high speed (65 000 rpm). Viewed through these new flat ends, the aerogels are perfectly transparent and display no macroscopic flaw. All four samples are enclosed in tightly fitting PMMA containers (apart from a 0–1 mm gap left open for the trapezoidal sample J_1).

An empty PMMA container, identical to that of aerogel A (diameter 12.5 mm, height 10.8 mm), is used as a reference cell for free diffusion measurements.

Polypropylene Luer fittings are glued to the PMMA containers to allow connection to the ^3He polarization system, through a 10-cm-long Tygon tube (Masterflex, Cole-Parmer Instrument Co., Vernon Hills IL, USA) with 1.6-mm inner diameter. A 0.7×1.1 -mm Teflon tube is inserted into the Tygon filling tube to reduce the dead volume. This also increases the gas flow impedance, hence limits the pressure change rates inside the aerogel sample.

There has been no attempt to clean the aerogels. The surface may have retained traces of preparation chemicals, as well as O_2 or moisture adsorbed during storage. During experiments, the samples are under vacuum, or in contact with high purity ^3He or N_2 gas. A totally negligible amount of He atoms may dissolve in the silica [27]. The aerogel behavior is controlled during and after use by visual inspection. Sample M remains clearly well attached to the glass walls. Several cracks are present in its bulk part, between the free surface and the top of the inner tubes that presumably provide mechanical support to the aerogel. They developed during prior use, due to rough filling and emptying procedures [37], but remained unaffected both by the breaking of one inner tube and the present series of measurements. All off-the-shelf samples (A, J_1 – J_4) are used for the first time. Through the PMMA side walls, J_1 and J_2 can be observed to expand and shrink slightly as pressure varies from 0 to 1 atm. Very few cracks developed inside these commercial aerogels, allowed to move freely inside the containers by an irreversible decrease of all their dimensions (by about 5%–10%) observed after a few pressure cycles.

B. NMR setup

The pulsed NMR experiments are performed at low frequency (62.4 kHz) using a homemade system, in the homogeneous static field used for optical pumping (OP) described in Section II C. We use free induction decay (FID) signals to monitor the ^3He magnetization, and spin-echoes generated by a standard Carr-Purcell-Meiboom-Gill (CPMG) sequence with an applied gradient to measure diffusion [46].

All NMR and gradient coils depicted in Fig. 1 are copper wire windings held by PMMA stands. They are sur-

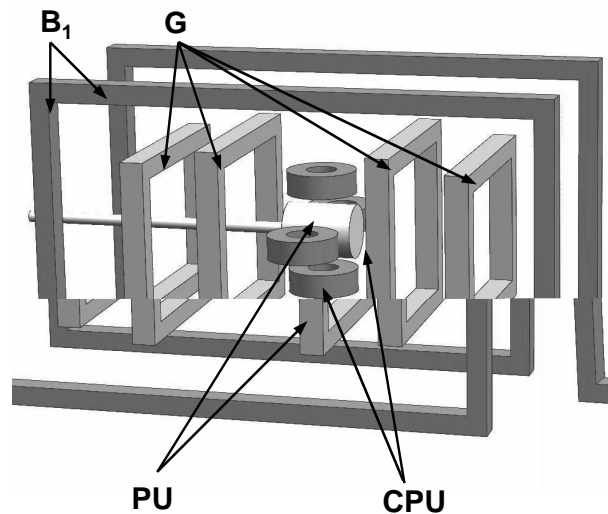


FIG. 1: Sketch of the NMR coils. G: set of four gradient coils (45×42 (45×35)-mm size, 4-mm horizontal width, 38 (78)-mm average spacing, and 9 (25) turns each, for inner (outer) coils, respectively; 0.75-mm diam. wire). B_1 : oversized induction coils (75×125 -mm size, 4-mm horizontal width, 52.5-mm average spacing, 25 turns each; 0.4-mm diam. wire). PU: pickup coils, and CPU: extra detection coils for rf noise compensation - see text - (10×18 -mm diam., 6-mm width, 440 turns each; 0.2-mm diam. wire). A thin filling tube is attached to the aerogel container (here depicted with cylindrical shape).

rounded by a closed copper box ($23 \times 16 \times 10 \text{ cm}^3$, thickness of 2 mm, not shown) for passive radio-frequency (rf) shielding. Two untuned, oversized rectangular induction coils are used to generate a very uniform rf field over the sample. Typically, a 90° tip angle is achieved by a 0.5-ms rf pulse with 11.5-V rms excitation. 180° pulses induce negligible magnetization losses, less than 10% after 1000 echoes refocused without applied gradient. Two circular detection coils lie in conventional Helmholtz configuration close to the sample (“PU” coils in Fig. 1). We use a pair of identical coils (“CPU” coils in Fig. 1), also implemented next to the sample and connected in opposition with the previous ones, to actively shield the device from pick-up noise. These two extra coils detect a noise signal from distant rf sources that almost exactly compensates for that induced in the main detec-

tion coils. Induction and detection coils are oriented so as to minimize the rf cross-talk, i.e., mutual induction. The set of detection coils is tuned to Larmor frequency with a parallel capacitor, and the quality factor is moderate ($Q=43$). The measured sensitivity corresponds to an expected 90° FID signal of $43\text{-}\mu\text{V}$ rms amplitude per mbar pressure and cm^3 of ^3He gas with 100% nuclear polarization. Two pairs of rectangular coils, connected in series, are designed to produce a uniform horizontal magnetic field gradient (25 mT/m/A) parallel to the static field axis. Computed relative variations over 3 cm around the center do not exceed 3%.

We use a dual-phase lock-in amplifier (LIA; model 7220, PerkinElmer Instruments, Oak Ridge Tennessee, USA) both to collect the NMR signal and to generate the resonant rf voltage. Rf pulse gating, dephasing, and amplification are handled by a personal computer (PC)-controlled home-built circuitry. Gradient and rf pulse sequencing, as well as data collection via an A/D converter (sampling frequency: 10 kHz), are managed using a laboratory-written software.

C. ^3He hyperpolarization system

^3He gas is hyperpolarized inhouse using the metastability exchange optical pumping technique. We use a home-built system that involves the basic units indicated by the block diagram in Fig. 2. The gas is polarized at a

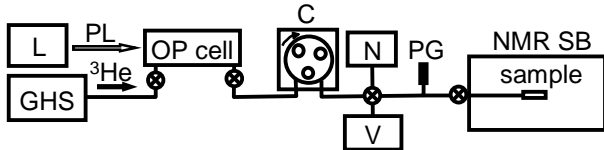


FIG. 2: Block diagram of the hyperpolarization system. L: laser source. GHS: gas handling system. PL: pump laser beam. OP cell: optical pumping glass cell. C: peristaltic compressor. N: Nitrogen gas supply. V: vacuum system. PG: pressure gauge. NMR SB: shielding box surrounding the sample and NMR setup sketched in Fig. 1.

pressure of about 2 mbars in a cylindrical glass cell (50-cm length, 6-cm diameter). The 1083-nm light source is a 2-W ytterbium fiber laser (model OI-FL1083-2W, Keopsys, Lannion, France). The OP beam is expanded and collimated (2-cm full width at half maximum), and circularly polarized. A mirror back-reflects it to enhance light absorption by the small fraction (typically 1 ppm) of ^3He atoms excited to the metastable state by a weak rf discharge (3-MHz frequency, 2-W power). A dedicated peristaltic compressor is used to extract the polarized gas from the OP cell and transfer it into the sample container [47]. Upstream of the OP cell, the gas handling unit (not shown) includes a ^3He bottle (purity grade higher than 99.99%), a getter to keep impurities level well below 1ppm (model GC50, SAES Getters, Lainate,

Italy), a high vacuum system (a turbomolecular pump backed by a membrane pump, electropolished stainless steel tubes and valves, pressure transducers), and an all-metal mass-flow regulator to control the gas flow into the OP cell. Downstream of the OP cell, the polarized gas is in contact with non-magnetic materials only (glass, Teflon, low-degassing plastic tubes, etc.). Leak-tight connections with respect to room air are required to avoid O_2 -induced relaxation [48]. Dead volumes are kept as small as possible, with the constraint that excess relaxation can result from drastic enhancement of surface-to-volume ratios.

A weak static magnetic field (2 mT) is generated by a set of six square coils of horizontal axis, designed to provide an optimal field homogeneity both for OP and NMR in a compact setup (Fig. 3). Relative inhomogeneities of

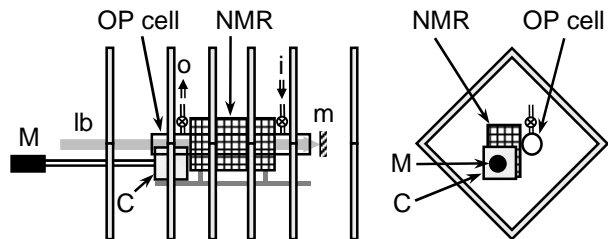


FIG. 3: Sketch of the ^3He hyperpolarization system (front and side views), showing the arrangement of OP cell, compressor (C), driving motor (M), and of the six square coils (average side length 40 cm, section $1.6\times 1.6\text{ cm}^2$) that provide the static field (0.8516 mT/A at the centre). Field map is optimized both for OP and NMR by coil positions (± 5.9 , ± 19.1 , and $\pm 37.8\text{ cm}$) and number of turns (85, 100, and 224, respectively). 2×30 additional turns are wired in opposite directions onto the outer square coils, yielding a 1.3 mT/cm/A shimming gradient over the sample. A mirror (m) back-reflects the laser beam (lb) into the OP cell, open at both ends for gas inlet (i) and outlet (o).

the applied field do not exceed a few parts per thousand over the entire cell volume for OP, and a few ppm over a 7-cm diameter spherical volume for NMR. The stray field inhomogeneity induced by the laboratory environment is weak, and local compensation of the dominant residual gradient is achieved using two shimming coils.

Absolute measurements of the nuclear polarization in the OP cell are performed by optical polarization analysis of the fluorescence light emitted by the plasma. With 2-W laser power, nuclear polarizations up to 60% can be obtained with no gas flow, and within the 30%–40% range around 1 sccm (standard cubic centimeter per minute) ($0.745\text{ }\mu\text{mol/s}$) flow rates, mostly due to pressure increase in the OP cell. The polarization losses in the compressor and connecting tubes, characterized in independent measurements [49], typically amount to 10%, at best.

D. Probe gas management

The filling tube attached to the aerogel sample is connected to a Luer polycarbonate stopcock valve located just outside the NMR shielding box. There, pressure (relative to the atmospheric pressure) is measured with a 1% accuracy in the 1 mbar–1 bar range using a piezoresistive sensor mounted in a nonmagnetic (plastic) case (Model 24PCCFA2G, Honeywell, Morriston NJ, USA). For low-pressure diffusion measurements, pure ^3He is used. The gas flows directly from the OP cell and is accumulated inside the aerogel by the compressor. For high-pressure diffusion measurements, accumulation of large quantities of polarized gas is of limited interest considering the bottleneck set to magnetization buildup by wall relaxation (see Section III B). Therefore, N_2 is used as a neutral, nonrelaxing buffer gas to slow down the diffusion of the ^3He atoms in the void spaces of the aerogels. The ^3He partial pressures vary from 10 to 200 mbars in the measurements, but most frequently no more than 30 mbars of polarized gas are introduced in the sample containers (i.e., only a few μmoles). Total pressures range from 10 mbars to 1 bar.

Before the NMR acquisition, the sample is flushed with pure N_2 (99.995% grade), then evacuated. Filling with polarized ^3He using the peristaltic compressor takes a few tens of seconds. Pure N_2 is optionally added to reach the targeted pressure value, then the measurement is performed. Right after signal acquisition, the gas is removed and the aerogel is kept under vacuum until the next measurement. Each series of measurements can last from a few hours to several days. When it is completed, the sample is open to room air and stored at ambient pressure.

III. NMR MEASUREMENTS

A. FID signals and line shapes

The performed measurements do not require an absolute calibration of the NMR detection system. However, we have used a small transmitting rf coil located at the center of the setup to probe the global pick-up sensitivity, and also to check that the ^3He signals correspond to nuclear polarization rates in agreement with those produced by the optical pumping system. The measured noise level is about $0.7\text{-}\mu\text{V}$ rms when the LIA time constant is set to minimum (160 μs). Nuclear polarizations vary from a few percents to 20% at best, due to relaxation in the aerogel, and the best spin-echo signal-to-noise ratios (SNRs) achieved are on the order of 30–50. Higher polarizations might be obtained if polarized gas is accumulated in a small glass cell, then rapidly expanded into the sample container. However, the procedure used here seems more suited to systematic and repeated measurements in the fragile silica substrates, and it still yields satisfactory accuracy.

In our experiments, FID signal lifetime is limited by residual field inhomogeneities due to the magnetic environment of the experiment after shimming (Section II C). The motional narrowing regime can then be fully reached for low pressure gas, and exponential decay is observed with a time constant T_2^* exceeding 2.5 s at 60-mbar pressure (whereas $T_2^* < 0.5$ s without shimming). At 1-bar pressure (no motional averaging) signal lifetime remains shorter, typically on the order of 0.2 s.

For the diffusion measurements, a strong gradient is applied so that at all pressures the FID lifetimes become much shorter and the line shapes, obtained by fast Fourier transform (FFT) of the NMR signals, are those imposed by the one-dimensional (1D) spatial distribution of resonance frequencies (see Section III C). Otherwise, line distortions occur due to diffusive relaxation or spectral edge enhancement effects [50, 51] and a variety of spectral profiles can be observed, depending on gradient amplitude (i.e., frequency span over the sample size) and gas pressure (i.e., diffusion time during observation) conditions. Particularly important in highly diffusive systems, these line distortion effects have recently been systematically characterized with good SNR using hyperpolarized noble gases [31, 52]. Care has thus been taken to select gradient strengths and echo times so as to avoid systematic biases in the diffusion measurements [50, 53–56].

B. Longitudinal relaxation rates

The contribution of dipole-dipole relaxation to the longitudinal relaxation time T_1 is totally negligible for pure ^3He (relaxation time inversely proportional to the ^3He pressure, exceeding 800 h at 1 bar [57]). Only severe contamination by air may play a significant role in our experiments, through strong dipole-dipole relaxation by the paramagnetic O_2 molecules (12.5 s at 1 bar and 21% oxygen concentration [48]). Bulk relaxation due to atomic diffusion in our residual field gradients is also negligible. Wall relaxation is thus the dominant process, and the magnetization lifetime depends on the nature of the materials in contact with the gas, and on the area of exposed surfaces.

The longitudinal relaxation time T_1 is measured to be 370 s in the empty machined PMMA cell. This corresponds to a specific relaxation time $\theta_s = T_1 A/V$ (A : area, V : volume) equal to 0.19×10^6 s/m, slightly lower than typical values reported for Pyrex glass ($\theta_s = 0.5 - 3.8 \times 10^6$ s/m [58–60]) and quartz ($\theta_s = 0.3 - 2.8 \times 10^6$ s/m [58, 61]).

Surprisingly long T_1 are measured in the aerogels, especially in the commercial ones, despite their huge nominal specific areas (a few tens of m^2 per cm^3) and uncontrolled cleanliness. T_1 reaches 130 s and 200 s in samples A and J₃, respectively. The contribution of the container walls can be estimated from the reference PMMA cell T_1 . This yields particularly weak spe-

cific relaxation times on the silica aggregates ($\theta_s = 6.6$ and 25×10^9 s/m, respectively), two orders of magnitude longer than the record values obtained with special aluminosilicate glasses (low-boron content Corning 1720 glass: 2.0×10^7 s/m [62]; Schott iron-free Supremax glass: $1.6\text{--}4.2 \times 10^7$ s/m [63, 64]). T_1 does not exceed 26 s in the custom-made sample M, which is less than initially measured at 2.3 mT (58 s) but more than subsequently obtained at 0.1 T (19 s) in the same sample [37]. Ferromagnetic impurities in the material [26, 58, 60] may be responsible for these hysteretic T_1 changes, also observed recently in bare glass cells exposed to high magnetic fields [64] (a phenomenon reported for rubidium-coated glass cells only, so far [65, 66]). Using an estimate for the Pyrex T_1 , and an approximate specific area ($22.9 \text{ m}^2/\text{cm}^3$ for a 98.2% similar custom-made aerogel [17]), the 58-s T_1 initially measured in sample M would still yield $\theta_s = 1.5 \times 10^9$ s/m for the silica aggregates (shorter than, but comparable to, that of the commercial aerogels). In all samples, magnetization decays are indeed slow enough to allow the one-shot CPMG diffusion measurements described hereafter.

C. Spin-echo attenuation

A 90_x° rf pulse (0.5-ms duration) is followed by a train of 180_y° rf pulses (1-ms duration) to refocus the transverse magnetization at a regular interval T_{CP} . CPMG measurements are made for different values of T_{CP} (6–31 ms) and of applied gradient G (0–2 mT/m). Spatially non-selective tipping is obtained with a good angle accuracy by switching off (on) the applied gradient 300 μs before (after) the beginning (the end) of the rf pulses.

For the CPMG sequence, the transverse magnetization has a decay time T_2' that can be written as

$$\frac{1}{T_2'} = \frac{1}{T_2} + \frac{1}{T_{2,\text{diff}}} \quad (1)$$

The first term on the right-hand side is the intrinsic relaxation rate of the system, that for the gas simply corresponds to the longitudinal decay rate ($T_2 = T_1$). This has been checked in the absence of applied gradient, using spin-echo trains with very short T_{CP} . The second term represents additional relaxation resulting from diffusion in a nonuniform magnetic field, due to an applied field gradient and/or the residual magnetic inhomogeneities after shimming.

For a uniform applied gradient G , $T_{2,\text{diff}}$ can be expressed in the case of free gas diffusion as

$$T_{2,\text{diff}} = \frac{12}{D(\gamma k G T_{\text{CP}})^2} \quad (2)$$

where D is the coefficient of diffusion and the factor k corrects for the time variation of the applied gradient, which is switched off during the rf pulses. For a rectan-

gular gradient pulse, this correction factor is:

$$k = \sqrt{\delta^2(3T_{\text{CP}} - 2\delta)/T_{\text{CP}}^3} \quad (3)$$

where $\delta \leq T_{\text{CP}}$ is the duration of the gradient [67].

All diffusion-weighted spin-echo trains are observed to decay exponentially. An example of spin-echo train and FFT is presented in Fig. 4. T_2' values are obtained from

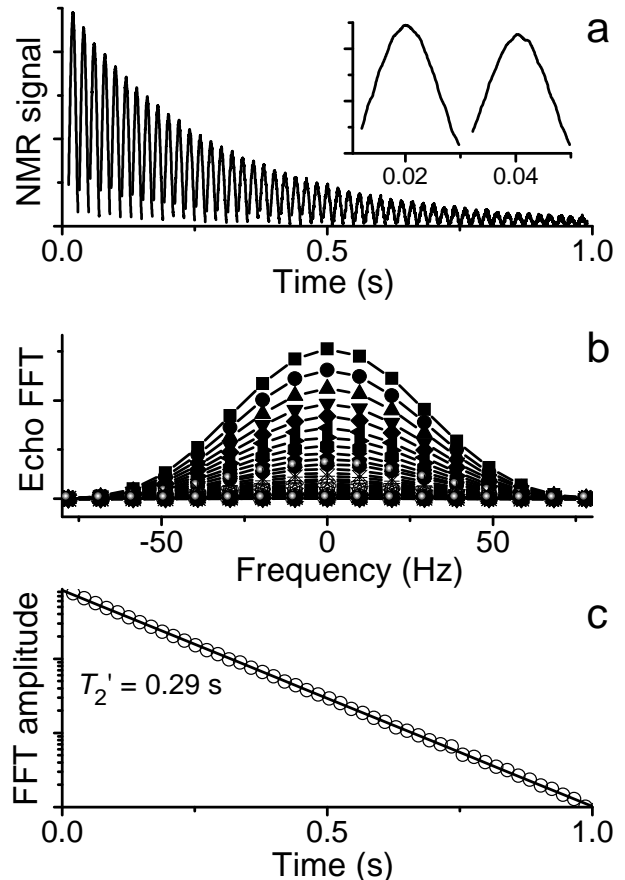


FIG. 4: a: Example of spin-echo train obtained in aerogel A (with 33.4 mbars of ^3He plus 616.5 mbars of N_2 , $G = 0.314$ mT/m, and $T_{\text{CP}} = 21$ ms). Saturation of the detection system by the strong rf pulses occurs between echoes (data points removed). Inset: Blow-up plot of first and second echoes. b: Fast Fourier transforms (FFTs) of the consecutive echo data sets, identified by individual symbol shapes. c: Exponential fit of FFT decay, yielding $T_2' = 0.29$ s.

monoexponential fits to the square of the echo amplitudes, or the square of their Fourier components. The use of power data, rather than magnitudes, yields a more reliable result as they are less sensitive to biases introduced by noise base lines [68].

The diffusion measurements are typically performed with short repetition times ($T_{\text{CP}} = 6$ or 11 ms) and finite gradients ($G = 0.4\text{--}1.2$ mT/m), and T_2' ranges from 25 to 1500 ms in aerogel (25 to 86 ms in the reference cell). The contribution of intrinsic T_2 to transverse relaxation is thus negligible at all pressures, and

$T'_2 = T_{2,\text{diff}}$. The frequency spectra of the recorded echoes provide 1D images of the gas magnetization in the samples (Fig. 5a). The shape of sample A is fairly

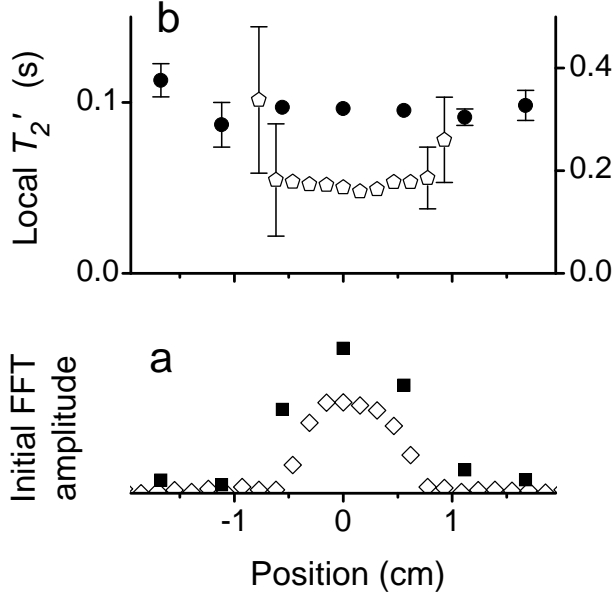


FIG. 5: Pixel-per-pixel analysis of frequency spectra, through monoexponential fits of the FFT decays, for spin-echo trains obtained in aerogels A (open symbols) and J₂ (solid symbols) with $G=1.56$ and 0.43 mT/m, respectively, and $T_{\text{CP}}=11$ ms. a: Local initial amplitudes (along gradient axis). Statistical error bars, not plotted, are less than 2% of the maximum amplitude. b: Local decay times (left axis: A; right axis: J₂). Statistical error bars are smaller than symbol sizes, except where plotted (i.e., on sample edges).

well reproduced considering the selected spatial NMR resolution $2\pi/(\gamma GT_{\text{obs}})=2.5$ mm ($\gamma=2\pi\times 32.43$ MHz/T is the gyromagnetic ratio of ³He nuclei, and T_{obs} the observation time that is very close to the gradient duration δ). Resolution is lower for the displayed J₂ profile (7.8 mm), but typical of most measurements presented in Section IV. The frequency spectra of the echoes also provide 1D maps of the decay time (Fig. 5b). Spatial variations ($\pm 10\%$) are small enough to accurately yield a single exponential T'_2 for the average magnetization.

From each measurement, a diffusion coefficient D is extracted using Eq. (2). Experimentally, the $1/T'_2$ data can be checked to exhibit the expected linear variation with $(kGT_{\text{CP}})^2$ at all pressures above 100 mbars. Fig. 6 displays, for instance, two series of measurements performed in the reference cell and in aerogel M at fixed gas pressures. Various combinations of parameters G and T_{CP} are used here, and in both cases all the data collapse on a straight line. In the empty reference cell, D coincides with the free-diffusion coefficient D_{gas} of the ³He atoms in the probe gas. In aerogel, D corresponds to an effective diffusion coefficient D_{eff} that describes the restricted diffusion of the atoms within the porous medium. Below 100 mbars, moderate departures

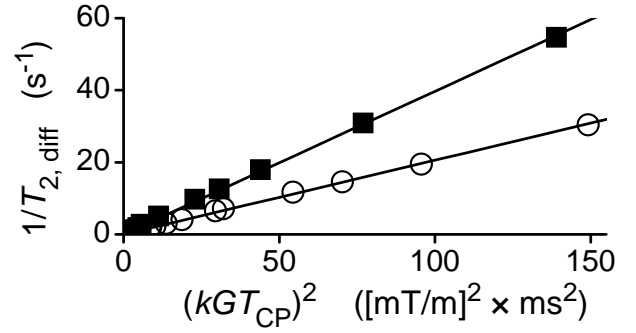


FIG. 6: Compilation of spin-echo decay rates measured in the reference cell (solid squares) and in aerogel M (open circles) at fixed gas pressures. Diffusion-weighting parameter $(kGT_{\text{CP}})^2$ is varied through changes of gradient strengths (G : 0.07–2.2 mT/m) and echo times (T_{CP} : 4.4–31 ms). The expected linear dependence [Eq. (2)], observed over more than two decades, yields $D_{\text{gas}} = 1.148 \pm 0.004$ cm²/s in the reference cell, and $D_{\text{eff}} = 0.595 \pm 0.008$ cm²/s in aerogel M, for the two ³He-N₂ mixtures used ($P_3^{\text{eq}} = 1.41$ bar and 1.70 bar, respectively - see Section IV A).

from the $(kGT_{\text{CP}})^2$ dependence can be observed in aerogel at high GT_{CP} , corresponding to reduced decay rates $1/T'_2$ (hence, overestimated values of D), typically above $kGT_{\text{CP}} = 4 \times 10^{-6}$ sT/m as reported in Ref. [39].

IV. RESULTS

A. Free gas diffusion

The free-diffusion coefficient D_{gas} for a ³He gas with partial pressure P_3 in a mixture containing N₂ with partial pressure P_{N_2} can be written as:

$$\frac{1}{D_{\text{gas}}} = \frac{P_3}{D_3(T)} + \frac{P_{\text{N}_2}}{D_{3\text{N}_2}(T)}, \quad (4)$$

where the reduced diffusion coefficients can be expressed as $D_3 = 1.967 \times (T/300)^{1.71}$ and $D_{3\text{N}_2} = 0.811 \times (T/300)^{1.65}$ in units of atm × cm²/s (1 atm = 1.013 × 10⁵ Pa), with the temperature T in Kelvin [36, 69]. Therefore, the scattering on N₂ molecules leads to an effect of the gas composition on atomic diffusion that can be accounted for using the *equivalent pressure* of pure ³He gas:

$$P_3^{\text{eq}} = P_3 + P_{\text{N}_2} \frac{D_3(T)}{D_{3\text{N}_2}(T)}, \quad (5)$$

with $D_3/D_{3\text{N}_2} = 3.462$ at 293 K. This allows to merge the results obtained in ³He–N₂ mixtures and in pure ³He gas. For free diffusion, $1/D_{\text{gas}}$ and hence T'_2 are expected to linearly depend on P_3^{eq} .

CPMG measurements performed in the reference cell are presented in Fig. 7. These data are obtained at

various ^3He pressures, with several combinations of parameters G and T_{CP} . They actually all collapse on a straight line when plotted as a function of the equivalent ^3He pressure P_3^{eq} . Moreover, the measured slope $5.06 \pm 0.04 \text{ mbar}^{-1} \times \text{s/m}^2$ (statistical error bar) is in fair agreement with the expected value ($1/D_3 = 5.23 \text{ mbar}^{-1} \times \text{s/m}^2$) given the 4% uncertainty due to long-term fluctuations of atmospheric pressure and temperature. This provides a consistency check for our apparatus, gradient assignment, and measurement technique.

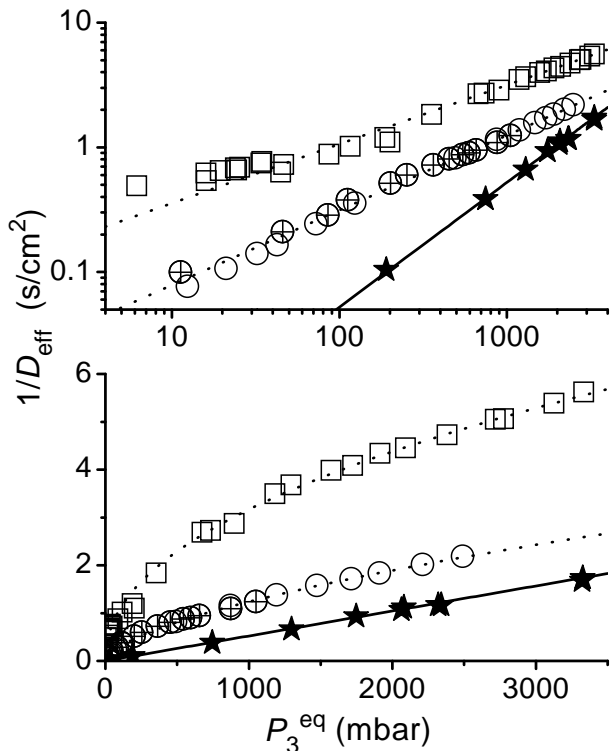


FIG. 7: Comparison of diffusion measurements performed in free gas, and in aerogels A and M. The same three sets of reduced data $1/D_{\text{eff}}$, plotted against pressure P_3^{eq} , are displayed in linear and logarithmic scales. Stars: reference cell data, free diffusion. Circles (respectively, squares): aerogel M (resp. A) data. Crossed circles: previous measurements in aerogel M [38, 39]. Solid line: linear fit of the free-diffusion data (slope: $5.06 \pm 0.04 \text{ mbar}^{-1} \times \text{s/m}^2$), in good agreement with the expected P_3^{eq}/D_3 dependence. Dotted lines: phenomenological power-law fits with exponents 0.47 (aerogel A) and 0.60 (aerogel M).

B. Gas diffusion in aerogel

Results obtained in aerogel samples A and M are also displayed in Fig. 7, so that they can be directly compared with the free-diffusion results. For clarity, the results obtained in samples J_1 – J_4 are presented separately in Fig. 8.

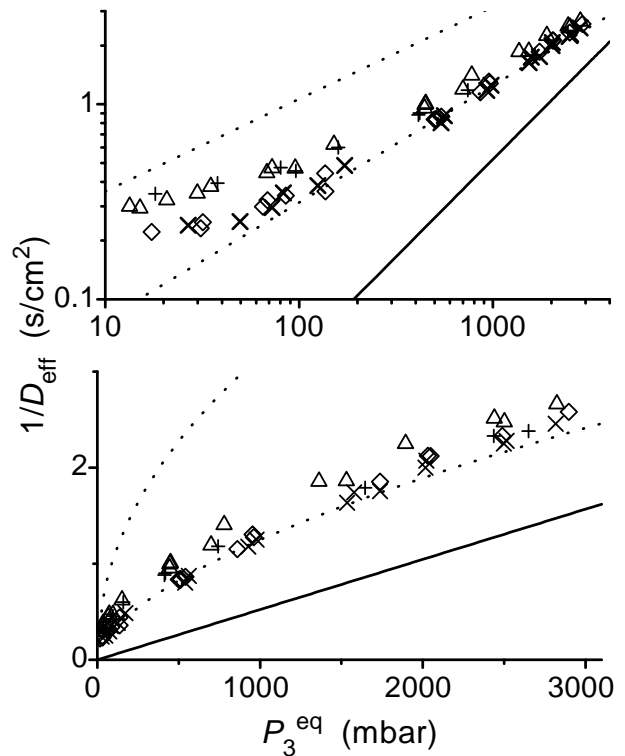


FIG. 8: Reduced diffusion data $1/D_{\text{eff}}$ as a function of P_3^{eq} for aerogel samples J_1 (plus signs), J_2 (open triangles), J_3 (open diamonds), and J_4 (crosses). Comparison is made with the linear fit of free-diffusion data (straight line), and power-law fits of aerogels A and M data from Fig. 7 (dotted lines). The J_1 – J_4 data can be consistently fitted by a power-law functions with exponents 0.53 or 0.64 (see Table I).

In Fig. 7, data from earlier measurements in sample M are also included for comparison. These measurements [38, 39] have been performed in a 0.1 T whole-body imager, using the broadband rf channel and the gradient system of that clinical unit. Homemade antennas were used for induction and detection at 3.24 MHz, as well as the in-house ^3He -NMR software for sequence management and data acquisition developed for *in vivo* lung studies [35, 70]. Pure ^3He gas was used for these CPMG measurements ($G = 0.21 \text{ mT/m}$, $T_{\text{CP}} = 10^{-2} \text{ s}$). Despite all these differences in apparatus and experimental conditions, the two sets of data are perfectly consistent. The present work significantly extends the probed range of gas pressures. It confirms both the global decrease in diffusion coefficient (as compared to free diffusion) and the strong nonlinear dependence on gas pressure. These results therefore appear to be quite robust, and reliably associated to intrinsic bulk characteristics of the aerogel (on which time or rough pressure variations seem to have no effect).

In Fig. 7, the results obtained in the other aerogel (A) are qualitatively similar but show a strikingly stronger departure from the free-diffusion behavior, revealing a much more restricted ^3He diffusion. This may be at-

tributed to the difference in aerogel porosities, the silica volume density being twice larger in A than in M. The quantitative difference in pressure dependences is emphasized by the logarithmic plot, that shows that the two sets of data are best fitted with distinct power laws.

Type J aerogel samples have exactly the same nominal porosity as A, and yet the data for J_1 – J_4 are actually much closer to those of M (see Fig. 8). Finally, data obtained in the four samples of type J are quite satisfactorily comparable, revealing only minor sample-to-sample variations (again, there is no sign of individual alteration by inflicted mechanical stress). These data are of lower quality, the SNR being lesser due to the smaller sizes of the J_1 – J_4 samples.

$1/D_{\text{eff}}$ exhibits a strong nonlinear pressure dependence in all aerogels. The logarithmic graphs in Figs. 7 and 8 show that the data can be described by simple power-law functions, with exponents lying in the 0.48–0.65 range. For aerogels A and J_1 – J_4 , the data depart from that common behavior (longer T_2' are measured) below 100 mbars, and this value is chosen as a lower bound for the fitting range. At the lowest pressures, limits of the validity domain of Eq. (2) (see Section III C) are indeed reached, due to the experimental conditions for measurements performed in these samples ($10^6 kGT_{\text{CP}} = 4.5$ and 6.1 Ts/m, respectively). With the choice made for sample M ($10^6 kGT_{\text{CP}} = 3.0$ Ts/m), no such departure occurs down to 10 mbars and all data are included in the power-law fit. Fit parameters are listed in Table I to sum up sample-to-sample variations.

V. DISCUSSION

The use of hyperpolarized ^3He is demonstrated to allow diffusion measurements with good accuracy, over a wide range of gas densities. The compact polarizer is perfectly suited to online preparation of the small gas quantities required to test the aerogel samples, and systematic measurements are easy to carry out and repeat. The high porosity samples under study are selected among silica aerogels that are most frequently used as host porous matrices for phase transition studies in low-temperature physics. None of these particular samples has been submitted to cool down-warm up, or compression-decompression, cycles comparable to those routinely performed in the low-temperature experiments. Exposure to high pressure or thermal stress has recently been demonstrated to induce irreversible changes in aerogels, that may macroscopically affect their structure [22]. It might thus be interesting to perform nondestructive NMR diffusion measurements in aerogel both before and after use at low temperature.

The consistent set of robust NMR data collected in the differently produced virgin samples reveals common bulk aerogel features, that are analyzed in terms of specific properties of the microscopic structure in this section. The unusually high porosities of the samples allow a par-

ticularly simple description of the gas kinetics inside the aerogels. Restricted diffusion is more often studied in denser media, where atoms or molecules are confined inside an ensemble of closed or interconnected pores that strongly constrains, by its geometry or tortuosity, the thermal motion of the probe species. In this work, the solid matrix occupies a very small fraction (1.5% to 3 %) of the volume of the aerogel, and the hyperpolarized ^3He atoms diffuse inside the widely accessible, huge space left open by the sparsely distributed silica aggregates.

Decay times of spin-echo amplitudes are measured to be two to five times longer in aerogel than in free gas. The decrease of the atomic diffusion coefficient is quite significant at pressures exceeding 1 bar, indicating that atom-atom and atom-silica collisions have comparable frequencies at these high gas densities. Surprisingly, a strong pressure dependence of D_{eff} is still observed at low pressures. As the probability of atom-atom scattering vanishes in a very dilute gas, the relative effect of pressure variations on the ^3He diffusion coefficient would be expected to become increasingly small at low pressures (and some characteristic length scale, if any, of the silica network should determine the finite value approached by the atom mfp at zero pressure - see Section V A). It is yet measured to remain large at low pressures, indicating that the free motion of the atoms is indeed allowed over large distances in aerogel (at 10 mbars, for instance, the mfp for free diffusion in ^3He is on the order of $40 \mu\text{m}$ [71]). This is systematically observed, in the custom-made aerogel sample and in the set of commercial ones that are obtained from two distinct manufacturers. It brings further support to the suggested nonuniform distribution of density of silica strands inside the aerogels, mentioned in the Introduction, that had been put forward to explain some preliminary results [38, 39].

The NMR gas diffusion data actually have two distinct features that compel description of the aerogel by more than a single characteristic length: the dominant power-law increase with pressure, and the departure from it that can be noticed at very low pressures. This departure has already been discussed in Ref. [39], and shown to be enhanced at large kGT_{CP} . As pressure decreases, the atomic diffusion gets more and more sensitive to scattering by the silica strands. This enhances the effects of spatial distribution inhomogeneities and the multiexponential nature of the spin-echo decay, as in other porous media [25]. The longest lived mode is favored for all length scales below the gradient-induced resolution, and monoexponential fits systematically lead to notably underestimated relaxation rates (i.e., increased $1/D_{\text{eff}}$ values). The following discussion focuses on the power-law dependence on pressure observed in all samples and on its analysis. Results are also compared to those obtained with other investigation techniques.

Sample	Manufacturer	Porosity [%]	Specific area [m ² /g]	Exponent β (stat. err.)	Prefactor [value for $P_3^{\text{eq}}=1$ bar] α (stat. err.) [s/cm ²]
M	custom made	98.5	-	0.60 (0.01)	1.25 (0.01)
A	Airglass	97	465	0.47 (0.01)	3.16 (0.03)
J ₁	Matsushita	97	510	0.53 (0.02)	1.42 (0.02)
J ₂	Matsushita	97	510	0.53 (0.02)	1.54 (0.02)
J ₃	Matsushita	97	510	0.64 (0.01)	1.31 (0.01)
J ₄	Matsushita	97	510	0.64 (0.02)	1.27 (0.02)

TABLE I: Characteristics and fit parameters for the six aerogel samples. Exponents (β) and prefactors (α) are obtained by phenomenological fits of the NMR diffusion data to $1/D_{\text{eff}} = \alpha \times (P_3^{\text{eq}})^\beta$, where $1/D_{\text{eff}}$ is in s/cm² and P_3^{eq} in bars (see text).

A. Crude model: uniform medium with a single characteristic mfp

The ³He diffusion process leading to spin-echo attenuation in the applied magnetic-field gradient can be viewed as a random walk in which free-flying atoms take successive individual steps that are terminated either by a collision with another gas atom or molecule (³He or N₂) or with silica. The frequencies of the two types of collisions being additive, the mfp λ_{eff} of this random walk can be related to the mfp λ_{gas} for gas collisions and λ_{aero} for collisions with the silica strands in a straightforward manner:

$$\frac{1}{\lambda_{\text{eff}}} = \frac{1}{\lambda_{\text{gas}}} + \frac{1}{\lambda_{\text{aero}}}. \quad (6)$$

The spatial distribution of silica is here assumed to be homogeneous, and the global effect of the aerogel structure on atomic motion is thus described by the single parameter λ_{aero} . The effective diffusion coefficient D_{eff} can then be written as:

$$\frac{1}{D_{\text{eff}}} = \frac{1}{D_{\text{gas}}} + \frac{1}{D_{\text{aero}}}, \quad (7)$$

where the first contribution (gas-gas scattering) involves the free-diffusion coefficient of ³He introduced in Section IV A, and the second one (³He–silica scattering) introduces the constant diffusion coefficient $D_{\text{aero}} = v\lambda_{\text{aero}}/3$, where v is the average thermal velocity ($v = \sqrt{8k_B T/\pi m}$; k_B : Boltzmann constant, m : atomic mass, T : temperature). The quantity $1/D_{\text{eff}}$ should therefore increase linearly with the gas pressure (or the equivalent pressure P_3^{eq} for a ³He–N₂ mixture), starting from a finite zero-pressure value that may vary from sample to sample with the degree of confinement of the ³He atoms by the silica network.

Over the wide range of the gas pressures investigated, the expected linear dependence on pressure is clearly not observed. This strongly rules out the description by a uniform density of silica scattering centres in the aerogels and an average mfp. Instead, a broad distribution of mean free paths at scales smaller than the imaging resolution has to be assumed to account for the experimental observations. This is quantitatively discussed in the following (Section V B), where the main features of

required mfp variations are correlated, over the probed range (0.1–40 μm), with the measured pressure dependences.

B. Phenomenological model: continuous distribution of mfp's in aerogel

To describe diffusion in heterogeneously distributed silica, a continuous distribution f of mfp's is introduced. The probability that the ³He-silica mfp λ_{aero} lies between λ_{aero} and $\lambda_{\text{aero}} + d\lambda_{\text{aero}}$ in some volume fraction of the sample is $f(\lambda_{\text{aero}})d\lambda_{\text{aero}}$. Assuming that the atoms rapidly exchange between regions of space characterized by different mfp's, the ³He magnetization is uniform and decays with a weighted average of local relaxation rates:

$$\frac{1}{T_{2,\text{diff}}} = \int \frac{f(\lambda_{\text{aero}})d\lambda_{\text{aero}}}{T_{2,\text{diff}}(\lambda_{\text{aero}})}. \quad (8)$$

Since the local relaxation times are given by:

$$T_{2,\text{diff}}(\lambda_{\text{aero}}) = \frac{12}{(\gamma k_G T_{\text{CP}})^2} \left(\frac{1}{D_{\text{gas}}} + \frac{1}{D_{\text{aero}}(\lambda_{\text{aero}})} \right), \quad (9)$$

the effective diffusion coefficient derived from the global decay time $T_{2,\text{diff}}$ using Eq. (2) reads:

$$\begin{aligned} D_{\text{eff}} &= \int \frac{f(\lambda_{\text{aero}})D_{\text{aero}}(\lambda_{\text{aero}})D_{\text{gas}}d\lambda_{\text{aero}}}{D_{\text{gas}} + D_{\text{aero}}(\lambda_{\text{aero}})} \\ &= \int \frac{f(\lambda_{\text{aero}})D_3 d\lambda_{\text{aero}}}{P_{\text{aero}}(\lambda_{\text{aero}}) + P_3^{\text{eq}}}. \end{aligned} \quad (10)$$

The physical quantity $P_{\text{aero}}(\lambda_{\text{aero}}) = 3D_3/v\lambda_{\text{aero}}$, that appears in the right hand side of Eq. (10), has the dimension of a pressure. It represents the contribution of the ³He-silica scattering process to hindering of atomic motion, on the λ_{aero} length scale, by the solid matrix. Eq. (10) shows that the integrand is a simple rational function of the probe gas pressure. The variations of D_{eff} with P_3^{eq} therefore put strong constraints on the mfp distribution f introduced in this model.

Experimentally, D_{eff} is proportional to $(P_3^{\text{eq}})^{-\beta}$ over a wide range of pressures. This is mathematically equivalent to set $D_{\text{eff}}(aP_3^{\text{eq}}) = a^{-\beta}D_{\text{eff}}(P_3^{\text{eq}})$, a being an arbitrary scaling constant. Through a straightforward

change from λ_{aero} to $a\lambda_{\text{aero}}$ as dummy variable in the integral [Eq. (10)], this relation can be shown to hold for all values of P_3^{eq} if, and only if, $f(\lambda_{\text{aero}}/a) = a^{2-\beta} f(\lambda_{\text{aero}})$. This translates into $f(\lambda_{\text{aero}}) \propto (\lambda_{\text{aero}})^{\beta-2}$. The mfp distribution, itself, corresponds to a power law, and its exponent is directly related to that measuring the $1/D_{\text{eff}}$ data scaling rate versus pressure. Although P_3^{eq} is varied over more than two decades, D_{eff} is actually measured over a finite pressure interval. Additional information would thus be required to fully characterize $f(\lambda_{\text{aero}})$. Yet, the distribution $f(\lambda_{\text{aero}}) \propto (\lambda_{\text{aero}})^{\beta-2}$ provides a convenient tool for quantitative analysis and discussion of the experimental results.

The effective diffusion coefficient can easily be computed from Eq. (10) using the distribution function $f(\lambda_{\text{aero}}) \propto (\lambda_{\text{aero}})^{-2+\beta}$, provided that f is suitably normalized. Since exponents β typically range from 0.5 to 0.7 in the aerogel samples under study, no divergence occurs at infinitely large λ , but some cutoff must be introduced at small λ to keep $\int f(\lambda)d\lambda$ finite. Numerical calculations are performed to probe the influence of both the upper and lower bounds of the mfp distribution, and to examine the constraints experimentally set by D_{eff} and its variation with P_3^{eq} in the 10 mbar–3 bar range. For simplicity, $f(\lambda_{\text{aero}})$ is assumed to be zero outside the interval $l < \lambda_{\text{aero}} < L$. Fig. 9 displays the results obtained at fixed β , arbitrarily set equal to 0.5, for different values of parameters l and L . As expected, the broader the mfp distribution, the closer to a power-law dependence is the variation of D_{eff} with pressure. Variations of the upper bound L lead to small changes of D_{eff} that can only be noticed at low pressures. These changes are found to be quite negligible above 10 mbars for L greater than 1 mm. The lower bound l has a much stronger impact. $1/D_{\text{eff}}$ increases when l is reduced, which corresponds to the aerogel hindering gas diffusion and restricting free paths to very short distances. On the contrary if, for instance, l is raised to 1 μm the atoms move almost freely inside the aerogel over the probed pressure range, and D_{eff} approaches D_{gas} . As the exponent of the pressure dependence exhibits no noticeable drift towards 1 at high pressure (log plot in Fig. 9), the experimental data definitely rule out $l > 30$ nm: mfp's on the order on a few nanometers must be encountered in all the aerogels under study.

Taking advantage of the weak impact of the upper bound L (all the more negligible since $P_3^{\text{eq}} < 100$ -mbar data have been discarded in the first of all samples but aerogel A), one can actually extract from the prefactor values α in Table I estimates for the smallest mfp encountered in each sample. Computing $1/D_{\text{eff}}$ as a function of l using Eq. (10) and the fit exponents β (L being conservatively set to 3000 μm), at fixed pressure $P_3^{\text{eq}} = 1$ bar, adjustments to the fit prefactors α yield results with quite reasonable orders of magnitude: $l = 29, 24, 22$ and 24 nm for samples $J_1, J_2, J_3,$ and $J_4,$ respectively; $l = 31$ nm for aerogel M; $l = 6.5$ nm only for aerogel A, where ^3He atoms experience the most restricted diffusion.

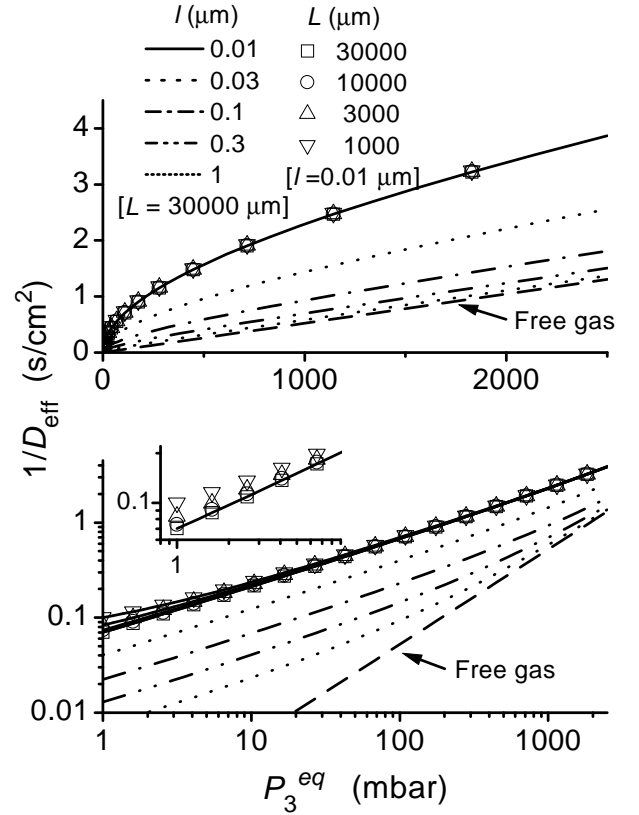


FIG. 9: Pressure dependence of $1/D_{\text{eff}}$ computed from Eq. (10) for broad power-law mfp distributions in aerogel $f(\lambda_{\text{aero}}) \propto (\lambda_{\text{aero}})^{\beta-2}$ with $\beta = 0.5$, as a function of lower (l) or upper (L) bounds. The mfp distributions range either from $l = 0.01 \mu\text{m}$ to $L = 1, 3, 10,$ and 30 mm (symbols), or from $l = 0.01, 0.03, 0.1, 0.3,$ and $1 \mu\text{m}$ to $L = 30$ mm (lines), as indicated in the legend. Dashed line: free diffusion limit. Inset: Blow-up of the log plot, focused on the small variations induced at low pressures by changes in upper bound L (at constant lower bound $l = 0.01 \mu\text{m}$).

More numerical results can be found in the supplemental material provided with this article through EPAPS [72]. In particular, shunt effects associated with the presence of macroscopic aerogel-free spaces inside the experimental cells are quantitatively investigated. Their impact is small for volume fractions below 10%, and would mainly result in a downwards curve bending at low P_3^{eq} that is not observed experimentally. Other types of broad mfp distributions (e.g., Gaussian, bimodal, and exponential distributions) are also easily ruled out, as computer calculations lead through Eq. (10) to a pressure dependence that is qualitatively very different from the observed one.

In summary, the spin diffusion measurements performed in aerogel strongly suggest a description of this particular medium by a broad range of mfp's with power-law statistical distribution. The global effect of silica network and its complex structure is best modeled with $f(\lambda_{\text{aero}}) \propto (\lambda_{\text{aero}})^{-\nu}$, with $1.3 < \nu < 1.6$ depending on

the investigated aerogel sample. Data analysis indicates that these distributions must extend at least from less than 30 nm to more than hundreds of micrometers.

C. Comparison with other studies

To our best knowledge, there is no comparable quantitative study of gas (self-)diffusion in aerogels [73]. Restricted gas diffusion has been reported in a recent attempt to probe aerogel pore-structure with imaging and spectroscopy NMR techniques using thermally polarized ^{129}Xe gas [74, 75]. A 3-fold decrease of the Xe diffusion coefficient is observed for pressures ranging from 1 to 30 bars, in several small specimens of unspecified origin and nominal characteristics. Other dense probe fluids can also be used to probe silica aerogels, e.g., water [76] or methanol [77]. But liquid phase NMR involves much shorter relaxation times and the quantitative analysis of the attenuation data is much less straightforward (spin-spin or spin-lattice relaxation processes must be taken into account [77]). Most reported ‘gas diffusion’ measurements [73] are gas phase studies that actually consist in transport measurements (permeametry), with assessment of gas flow through virgin [78–81] or partially densified [80, 82, 83] aerogels. In this case, a mean pore size of the interconnected open network is usually inferred from measured flow rates of gas through the pores using a suitable geometrical model of the open system.

Flow measurements actually provide information about the structure of the porous matrix in the Knudsen regime, i.e., at low enough pressure, when free molecular diffusion dominates. The gas-flow conductance then becomes pressure independent, and it is solely determined by the cumulative effect of collisions on the silica walls [83–86]. The standard capillary-bundle model for porous media appears to give an acceptable description of both static or dynamic flow experiments in aerogel [78–80, 82]. Using a tortuosity coefficient τ to account for the pore morphology and connectivity of the pore network, the diffusion coefficient is written as $D_{\text{eff}} = D_{\text{Kn}}/\tau$ with reference to the Knudsen diffusion coefficient D_{Kn} in straight parallel, non-overlapping cylindrical pores of infinite length. In this model $D_{\text{Kn}} = v\phi/3$, where the tube diameter ϕ is equal to the characteristic size of the real pore structure under consideration (e.g., the hydraulic diameter, or mean intercept length). The ϕ values derived from these molecular flow measurements range from 10 to 50 nm, in agreement with the hydraulic diameters computed from standard stereology: $\phi = 4\epsilon/\rho\Sigma$ (ϵ : porosity, ρ : density, and Σ : specific area) or the mfp’s obtained from SAS measurements [80, 82]. And the effective diffusion lengths are 1.4 to 3 times larger than for straight line motion, due to tortuosity [79, 80].

Extending the capillary-bundle model to the aerogels used in the present work, in the Knudsen regime one would expect diffusion coefficients on the order of $0.6 \text{ cm}^2/\text{s}$ for samples of both type A and J, since the

hydraulic diameters computed from their commercially specified specific areas and densities are quite comparable for these two ($\phi=127$ and 116 nm , respectively). The large differences in D_{eff} experimentally observed by NMR at all pressures, in the two types of aerogel, suggest that either (1) the effective pore size derived from the capillary-bundle model suited for the analysis of flow measurements is not relevant to characterize the influence of the complex ramified silica network on pure self-diffusion in the gas, or (2) the structure of the aerogel matrix in the high porosity samples under study is very different from that of most aerogels used in the above-quoted references.

In several experiments, the Knudsen regime is reported to be reached for average gas pressures typically below 1 bar for aerogel densities ranging from 0.1 to 2.2 g/cm^3 [80, 82]. However, a clear transition from molecular to viscous flow has once been observed around 150 mbars in a 0.28-g/cm^3 sample (yet, the authors computed an effective pore radius on the order of $19 \mu\text{m}$, using a modified capillary-bundle model) [78]. Moreover, a similar observation can be found in one recent systematic study devoted to samples from an aerogel monolith grown with comparably high porosity (density 0.06 g/cm^3 ; area $800 \pm 30 \text{ m}^2/\text{g}$) [81]. Interestingly enough, the conclusion drawn from flow measurements performed in that study is that “the absence of any clear break (in the transition from diffusive to viscous flow) supports the assumption of a continuous distribution of pores sizes within the range of mean free paths in this experiment”. The experiment was actually performed with He mfp’s ranging from 90 to $3.5 \mu\text{m}$ (measurements were also repeated with N_2 gas, for mfp’s ranging between 30 and $1 \mu\text{m}$, and a similar behavior has been observed). Furthermore, this analysis correlated with an intriguing “significant pore volume (detected) throughout the measuring range of the instrument from 2 to 200 nm ” (by nitrogen desorption isotherm technique) [81]. Hence, the upper and lower boundaries of the continuous pore size distribution assumed for the high porosity aerogel specimens investigated in Ref. [81] are quite comparable to those derived in the present NMR work for ^3He (self-)diffusion mfp’s, using the power-law distribution model presented in Section V B.

VI. CONCLUSION AND PROSPECTS

In summary, laser optical pumping has been combined with low field NMR to nondestructively probe high porosity aerogel samples, by spin-echo diffusion measurements with hyperpolarized ^3He gas. Analysis of the diffusion data has been based on a statistical description of the gas motion inside the solid matrix. Restricted diffusion has been related to ^3He mfp changes induced by interactions between the probe atoms and the sparsely distributed silica strands, a gas kinetics approach particularly suited to the widely open aerogels under study. The experimental

findings are satisfactorily accounted for, assuming broad mfp's distributions inside the aerogels with ranges and power-law probability weights that are determined from the pressure dependence of the measured effective diffusion coefficients.

The conclusions drawn from our study support the idea that these high porosity aerogels are not well-defined systems. It may hence contribute to cast doubt on simple models and interpretations of low-temperature physics experiments, and fosters the growing concern that they may not be ideal host media when high control of induced confinement and disorder is required. Moreover, some aspects of the methodology and experimental techniques that have been used may be directly applied, or extended, to a variety of other porous systems, as follows.

In our work, a buffer gas (N_2) has been used to slow down 3He diffusion in the aerogel void spaces, and to achieve a significant increase of the pressure measurement range. This is applicable in all systems where the gas pressure cannot be increased *ad libitum*. For instance, diffusion imaging of inhaled hyperpolarized 3He gas is currently used to observe in human lungs spatial variations of alveolar size related to physiology [36, 87], posture [88], respiratory conditions [89], or disease [89–91]. Operation at atmospheric pressure being mandatory *in vivo*, mixing with biologically inert heavy buffer gases may be advantageously used to enhance contrast for such studies (e.g., SF_6 decreases the 3He diffusion coefficient by a factor up to 4 at 1 bar, depending on dilution) but also, more generally, to reduce diffusion-weighted attenuation by encoding gradients for improved SNR sensitivity and image quality [92].

Using hyperpolarized 3He , we have been able to probe our aerogel samples over a very broad range of diffusion lengths with the same measurement technique. This provides a powerful alternative to standard NMR approaches, often limited by technical aspects (e.g., acquisition rates, gradient amplitudes or ramping times), provided that the pressure can be directly varied by several orders of magnitude in the porous medium. Application to denser silica aerogels is straightforward, but may be considered as well for other rigid porous systems allowing fast gas diffusion. For instance, diffusion measurements could be considerably extended *in vitro*, using fixed lungs with preserved air spaces [92], to bridge the gap between conflicting *in vivo* lung investigations performed on time scales ranging from a few milliseconds to tens of seconds (using gradient echo [89, 90], spin echo [35] and spin tagging [93, 94] techniques), and to clear up the link between 3He NMR data and airways structural characteristics [95–97].

Laser polarization of the probe gas actually yields high SNRs to perform highly accurate NMR measurements in a variety of model systems (single pores [56, 98], rocks [99] or packed glass beads [99, 100]). The technique yet requires that a sufficiently large nuclear polarization is preserved inside the porous medium. This potentially limits the type of materials that can be probed, at least

in the static mode operated here. However, for materials with moderately low specific relaxation times, continuous flow techniques can be used to maintain a suitable stationary magnetization, through replenishment by freshly polarized gas. Most demonstrations involve hyperpolarized xenon gas so far [100, 101], but flow measurements are also very easy to perform with the compact 3He gas production system described in Section II C.

Finally, a specific interest of operation at low magnetic field may be emphasized. Interpretation of NMR diffusion data is known to crucially depend on adequate background gradient compensation, but also on the predominance of applied gradients over internal ones. In our work, local-field inhomogeneities due to the aerogel matrix were irrelevant for the analysis of the measurements. But NMR studies with hyperpolarized gas are highly sensitive, and they may equally reveal weak bulk magnetic susceptibility effects (e.g., the influence of glass containers at high field [31]) or artifacts generated by dominant susceptibility-induced field gradients (e.g., in ventilation imaging at 1.5 T [33, 34]). Operation at low or ultralow field can be very helpful to separate the effects of applied and local gradients for improved quantitative understanding in complex porous systems, as recently demonstrated in lungs [35, 36, 87].

Acknowledgments

Sample M has been kindly prepared for us by Norbert Mulders in Moses Chan's laboratory at Pennstate University. Similar custom-made aerogels are used for low-temperature experiments at UPenn, Cornell and Northwestern Universities, and several other places. Samples A and J_1 – J_4 have been provided by Georg Eska, Bayreuth University.

Supplemental material: EPAS Document E-JCPSA6-123-034528 [72]

All the notations used in this supplemental material are those introduced in the related article.

The first section investigates the effects of macroscopic void (aerogel-free) spaces present in the experimental volumes on the NMR diffusion measurements with hyperpolarized 3He gas. The probe atoms are strongly confined inside the aerogel, but diffuse freely (hence, much faster) in these void spaces. If the contribution of such diffusion “shunts” to the spin-echo attenuation is significant, the global effective coefficient D_{eff} extracted from the NMR data must differ from that of the bulk aerogel. Shunt effects are quantitatively assessed, and discussed as a function of the volume fraction of open void spaces.

The second section provides examples of computed effective diffusion coefficients in bulk aerogel, for a few kinds of broad mfp distributions. Results are successively presented for Gaussian, bimodal, and exponential distri-

butions. They contrast strongly with those obtained with the power-law distributions used in the article, that satisfactorily describe the experimental diffusion data.

A. Shunt effects

Experimentally, the void spaces open to ^3He diffusion may be large cracks that have developed inside the aerogel samples, or gaps between the bulk material and the container walls for aerogel samples that do not fill up the whole cell volume.

A finite fraction x of the sample volume where mfp λ_{aero} gets infinite is introduced to describe such a macroscopic ‘‘aerogel-free’’ region of space, where the atoms are free to move. As in Section V-B of the related article, fast exchange is assumed between this region and the bulk aerogel, leading to an effective diffusion coefficient that can be written as:

$$D_{\text{eff}} = (1 - x) \int \frac{f(\lambda_{\text{aero}}) \mathcal{D}_3 D_{\text{aero}}(\lambda_{\text{aero}}) d\lambda_{\text{aero}}}{\mathcal{D}_3 + D_{\text{aero}}(\lambda_{\text{aero}}) P_3^{\text{eq}}} + x \frac{\mathcal{D}_3}{P_3^{\text{eq}}}. \quad (\text{S-1})$$

Fig. 10 shows the variations of $1/D_{\text{eff}}$ with the void fraction x , for a fixed mfp distribution in aerogel (ranging from 10 to 30 nm, with $\beta = 0.5$). For all pressures, triv-

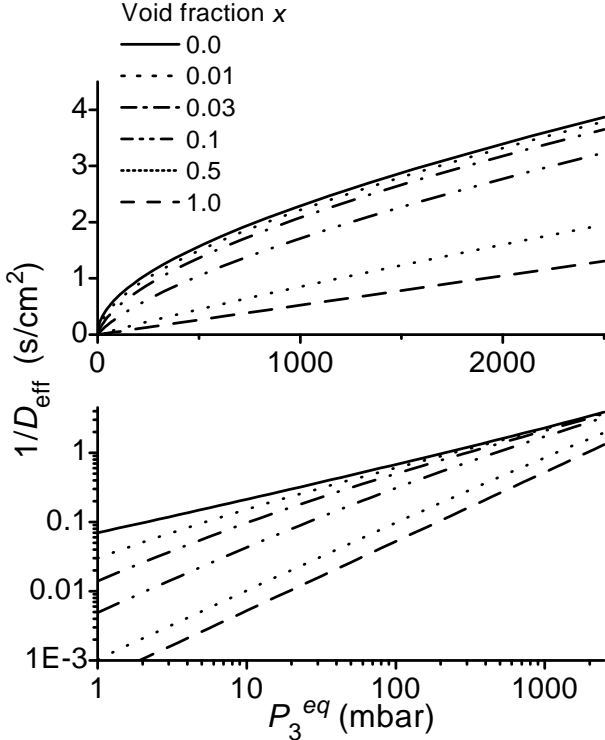


FIG. 10: Computed pressure dependence of $1/D_{\text{eff}}$ as a function of the void fraction x [Eq. (S-1)], for a mfp distribution in aerogel $f(\lambda_{\text{aero}}) \propto (\lambda_{\text{aero}})^{\beta-2}$ with $\beta = 0.5$, ranging from $l = 10$ nm to $L = 30$ nm.

ially, D_{eff} increases towards D_{gas} as x increases. However, large global changes of $1/D_{\text{eff}}$ (i.e., of spin-echo de-

cay times) occur only for $x > 10\%$. The changes induced by the void fraction are relatively larger at lower pressures. At small x , the log plot indicates that they translate into a significant downwards bending of the curves at low P_3^{eq} that is not observed experimentally. At intermediate x , the pressure dependence is strongly altered over the whole pressure range, and cannot be satisfactorily described by a single power-law variation.

In the custom-made aerogel M (grown-in sample, attached to the glass walls), the void fraction corresponding to the visually observed cracks is very likely to be extremely small. Since no significant departure from the power-law fit is observed in the data down to $P_3^{\text{eq}} = 10$ mbars, their actual contribution to D_{eff} is negligible.

Void spaces are larger in the commercial aerogel samples. Some have shape imperfections (e.g., small pieces of material missing on the corners, and irregular edge surfaces) that leave macroscopic open spaces with dimensions below 1 mm. All samples, irreversibly shrunken after a few pressure cycles, no longer occupy the whole volume of the containers. Conservative estimates for the volume fraction x hardly reach 10%–20%. The largest void fraction must be that of sample J_1 (crushed sample with trapezoidal shape, already not matching its container in thickness). But, the exponent associated to the pressure dependence measured in aerogel J_1 is actually smaller than those obtained in aerogels J_2 and J_4 , and not larger.

All this supports our belief that the measured features can trustfully be assigned to be those of bulk aerogel.

B. Diffusion coefficients computed for various mfp distributions.

The expected pressure dependence of $1/D_{\text{eff}}$ can easily be computed for any type of normalized mfp distribution function using Eq. (10) of the related article. The expression of the effective diffusion coefficient may be slightly modified by simple algebra (using $P_{\text{aero}}(\lambda_{\text{aero}}) = 3\mathcal{D}_3/v\lambda_{\text{aero}}$), to let the rational function of pressure and mfp involved in the integrand appear more explicitly:

$$D_{\text{eff}} = \int \frac{f(\lambda_{\text{aero}}) \mathcal{D}_3 d\lambda_{\text{aero}}}{P_{\text{aero}}(\lambda_{\text{aero}}) + P_3^{\text{eq}}} = \frac{\mathcal{D}_3}{P_1} \int \frac{f(\lambda) \lambda d\lambda}{\lambda_1 + \lambda (P_3^{\text{eq}}/P_1)} \quad (\text{S-2})$$

where P_1 is an arbitrary reference value for pressure, and $\lambda_1 = 3\mathcal{D}_3/vP_1$ the corresponding mfp for free diffusion (e.g., $\lambda_1 = 399.2 \mu\text{m}$ at 293 K for $P_1 = 1$ mbar). Some examples are briefly discussed below (Gaussian, bimodal and exponential distributions), to show the qualitative differences between these computed pressure dependences and the experimentally observed features.

For convenience, all computed values of $1/D_{\text{eff}}$ are discussed in terms of $P_{\text{eff}} = \mathcal{D}_3/D_{\text{eff}}$ (the pressure of freely diffusing ^3He gas required to yield a diffusion coefficient value equal to D_{eff}). Hereafter, the probing gas pressure is also simply designated by P_3 (equal to the actual

pressure for pure ^3He gas, or to the equivalent pressure P_3^{eq} for a gas mixture as described in the text for the $^3\text{He} - \text{N}_2$ mixtures used in the experiments).

1. Gaussian mfp distributions

Figs. 11 and 12 display the results obtained for Gaussian mfp distributions characterized by mean values λ_0 and widths $\delta\lambda$.

A narrow Gaussian distribution leads to a variation of P_{eff} that is very similar to that described in Section V-A of the related article for a uniform medium with a single characteristic mfp λ_{aero} equal to λ_0 . For instance, selected data from computations performed for various mean values λ_0 and constant width $\delta\lambda$ are presented in Fig. 11. The linear plot in Fig. 11 shows that, for each

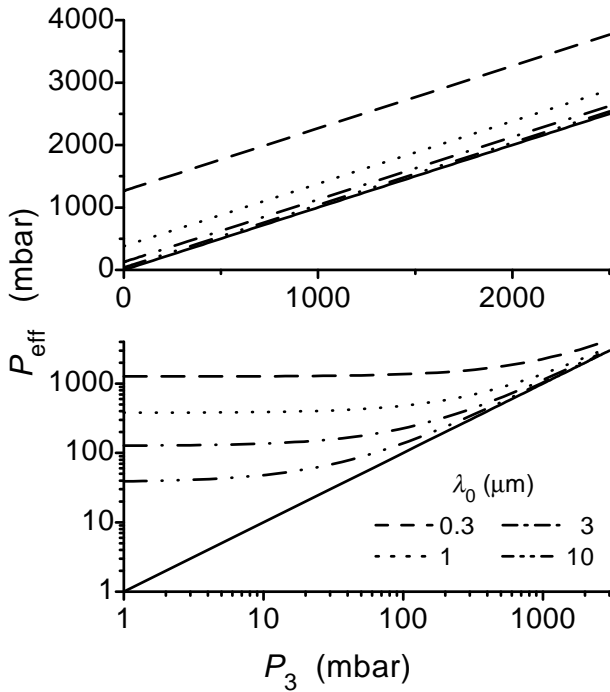


FIG. 11: Broken lines: Pressure dependence of $P_{\text{eff}} = \mathcal{D}_3/D_{\text{eff}}$ [Eq. (S-2), with $f(\lambda) \propto \exp[-(\lambda - \lambda_0)^2/\delta\lambda^2]$], computed for various mean values λ_0 (see legend) and $\delta\lambda = 0.01 \mu\text{m}$. Solid line: free gas data ($P_{\text{eff}} = P_3$).

λ_0 , P_{eff} actually scales linearly with P_3 with an offset value that increases as λ_0 decreases. With $\delta\lambda = 0.01 \mu\text{m}$, over the probed pressure range, all curves can be fit by straight lines with slopes equal to 1 and offset values $P_{\text{eff}}(0) = 3\mathcal{D}_3/v\lambda_0$ with an accuracy better than 50 ppm. The log plot in Fig. 11 therefore exhibits, for each value of λ_0 , a crossover from the free gas behavior (solid line) at high pressure, to a plateau at low pressure (where the mfp for free diffusion becomes so large that the effective mfp is just that imposed by the aerogel, λ_0). This crossover occurs when the mfp $\lambda_{3\text{He}}$ for gas collisions becomes comparable to λ_0 (i.e., around $P_3 = 3\mathcal{D}_3/v\lambda_0$).

The crossover region typically extends over one decade in pressure.

The influence of the width $\delta\lambda$ is depicted in Fig. 12, where λ_0 is kept constant and $\delta\lambda$ is varied ($\lambda_0 = 0.3 \mu\text{m}$; $\delta\lambda = 0.01$ to $30 \mu\text{m}$). The impact of the Gaussian width

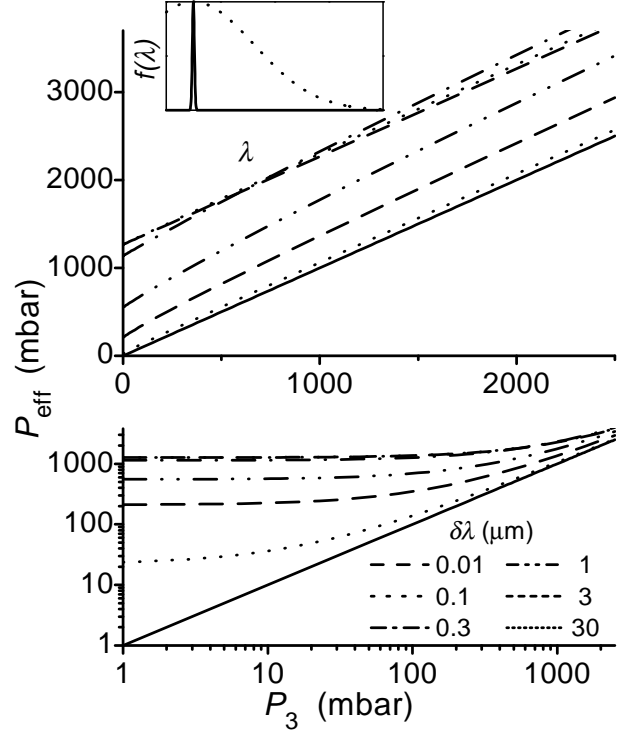


FIG. 12: Broken lines: Pressure dependence of $P_{\text{eff}} = \mathcal{D}_3/D_{\text{eff}}$ for Gaussian mfp distributions in aerogel [Eq. (S-2), with $f(\lambda) \propto \exp[-(\lambda - \lambda_0)^2/\delta\lambda^2]$], computed for various widths $\delta\lambda$ (see legend) and constant mean value $\lambda_0 = 0.3 \mu\text{m}$. Solid line: free gas diffusion ($P_{\text{eff}} = P_3$). Inset: Illustration of two extreme cases: broad (dashed line) and narrow (solid line) Gaussian mfp distributions. For the broad one, truncation at $l = 0$ leads to an average mfp that is significantly higher (hence, to less restricted atomic diffusion).

is quite small as long as $\delta\lambda \leq \lambda_0$, and corresponds to a slight change of the effective slope (linear plot in Fig. 12: dash, dot, and dash-dot lines). A significant change occurs when $\delta\lambda$ becomes comparable to λ_0 , due to truncation at small $\delta\lambda$. This situation is qualitatively depicted by the inset in Fig. 12 that displays Gaussian distribution profiles for $\delta\lambda \ll \lambda_0$ (solid line) and for $\delta\lambda > \lambda_0$ (dashed line). For a further increase of the Gaussian width, the impact becomes more significant since much larger mfp's are reached (looser spatial confinement of the atoms), and a strong offset decrease is observed for $\delta\lambda \gg \lambda_0$ (linear plot in Fig. 12: dash-dot-dot, short dash, and short dot lines). For instance, in spite of the short mfp mean value selected here ($\lambda_0 = 0.3 \mu\text{m}$), the free-diffusion limit would nearly be recovered over the experimentally probed pressure range (i.e., $P_3 > 10$ mbars, and hence $\lambda_{\text{gas}} < 40 \mu\text{m}$) for $\delta\lambda$ on the order of $30 \mu\text{m}$ (log plot in Fig. 12).

As a conclusion, whatever the choice of numerical parameters, a Gaussian distribution fails to provide a suitable pressure dependence to account for the experimental measurements.

2. Bimodal mfp distributions

Figs. 13 and 14 illustrate the expected behaviors for bimodal distributions that are sums of two Gaussian functions with identical amplitudes.

In Fig. 13, a narrow Gaussian distribution $f^{(1)}$ ($\lambda_0 = 50 \mu\text{m}$, $\delta\lambda = 0.1 \mu\text{m}$) is combined with another narrow Gaussian distribution (mean: $10 \mu\text{m}$, width: $0.1 \mu\text{m}$). As

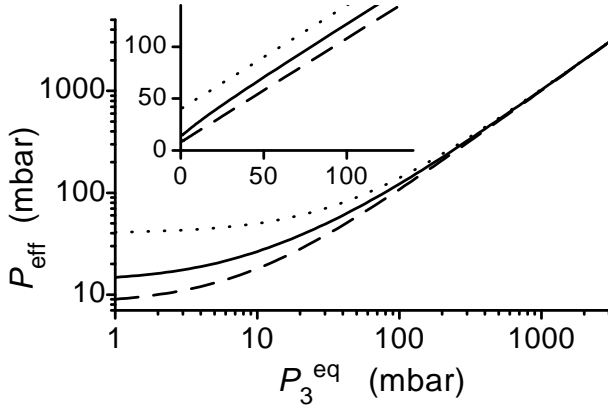


FIG. 13: Pressure dependence of P_{eff} obtained for a bimodal mfp distribution (solid line) that combines two narrow Gaussian distributions: $\lambda_0 = 50 \mu\text{m}$, $\delta\lambda = 0.1 \mu\text{m}$ (distribution $f^{(1)}$, dashed line), and $\lambda_0 = 10 \mu\text{m}$, $\delta\lambda = 0.1 \mu\text{m}$ (dotted line), in log plot. Inset: linear plot, for the same distributions.

expected, the dominant contribution arises from the distribution that provides access to the largest mfp's. The relative difference between the bimodal distribution and the $f^{(1)}$ Gaussian distribution is noticeable at low pressure. The combination with the other Gaussian results in a significant offset increase (70% change), and a slight curve distortion below $P_3 = 100$ mbars (best seen in the inset). The corresponding relative change in P_{eff} values is plotted against gas pressure in Fig. 14 (solid line). It becomes negligible as soon as the free gas mfp gets smaller than the lowest bound of the mfp distribution in aerogel.

Fig. 14 also displays results obtained for different values of the width $\delta\lambda$ of the $f^{(1)}$ Gaussian distribution, that remains centered around $\lambda_0 = 50 \mu\text{m}$. The relative impacts of the combination with the other Gaussian distribution can be checked to become smaller as the width $\delta\lambda$ is increased, due to the reduced relative weight of this additional contribution (Fig. 14, broken lines).

Whatever the combination of Gaussian distributions performed, bimodal distributions can absolutely not be adjusted to match the power-law pressure dependence that is experimentally observed.

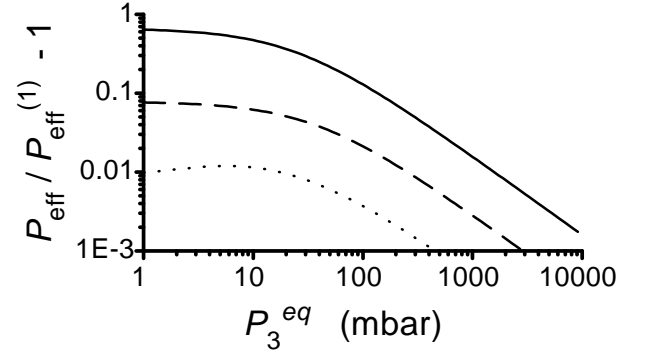


FIG. 14: Pressure dependence of the relative changes in P_{eff} for bimodal mfp distributions obtained by combination of Gaussian distributions $f^{(1)}$ centered around $\lambda_0 = 50 \mu\text{m}$ with various widths $\delta\lambda$ (providing the reference values $P_{\text{eff}}^{(1)}$), and a fixed Gaussian distribution (mean: $10 \mu\text{m}$, width: $0.1 \mu\text{m}$). Solid line: $\delta\lambda = 0.1 \mu\text{m}$ (value identical to that used in Fig. 13). Dashed line: $\delta\lambda = 1 \mu\text{m}$. Dotted line: $\delta\lambda = 10 \mu\text{m}$.

3. Exponential mfp distributions

Fig. 15 displays the pressure dependences typically obtained for exponential distributions with characteristic mfp's λ_c ranging from $0.05 \mu\text{m}$ to $1 \mu\text{m}$ (identified by distinct line styles in the graph). P_{eff} remains finite at

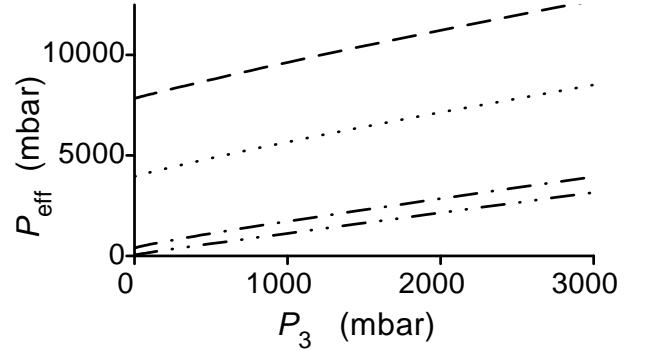


FIG. 15: Pressure dependence of P_{eff} for exponential mfp distributions [Eq. (S-2), with $f(\lambda) \propto \exp(-\lambda/\lambda_c)$] for various characteristic mfp's λ_c : $0.05 \mu\text{m}$ (dashed line), $0.1 \mu\text{m}$ (dotted line), $1 \mu\text{m}$ (dash-dot line), and $10 \mu\text{m}$ (dash-dot-dot line).

very low pressures and approaches $P_{\text{eff}}(0) = 3\mathcal{D}_3/v\lambda_c$, the expected value for an unbounded distribution. P_{eff} also increases with pressure, but not linearly. The derivative dP_{eff}/dP_3 smoothly varies between two asymptotic values: 2, at null pressure, and 1, at infinite pressure. For each P_{eff} curve, the change of local slope essentially occurs over the pressure range where the mfp for free diffusion is larger than (or equal to) the characteristic scale λ_c introduced by the aerogel. Beyond this limit, the gas motion is hardly limited by the solid matrix. This nearly-free diffusion regime (linear pressure dependence with slope 1) is reached for $P_3 \gg 40$ mbars at $\lambda_c = 10 \mu\text{m}$, for instance. At $\lambda_c = 0.05 \mu\text{m}$, the probed pressure range

must be extended to $P_3 \gg 8$ bars to observe it (data not shown in Fig.15).

When a lower bound l is arbitrarily set to the exponential mfp distribution, the results for P_{eff} are strongly altered (Fig.16). Since all mfp's smaller than l are re-

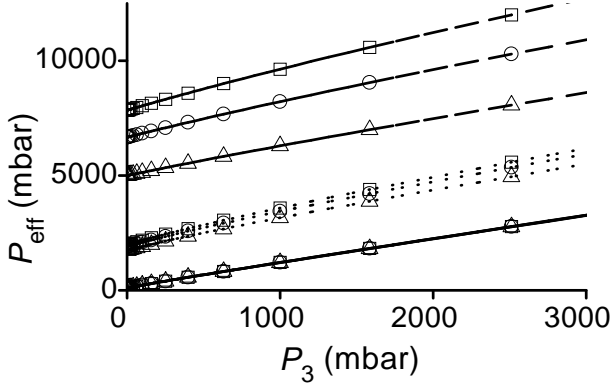


FIG. 16: Pressure dependence of P_{eff} for truncated exponential mfp distributions. Computations are performed for three values of the characteristic mfp λ_c : $0.05 \mu\text{m}$ (dashed lines), $0.2 \mu\text{m}$ (dotted lines), and $5 \mu\text{m}$ (solid lines). For each λ_c value, three different lower bounds l are set to the mfp distribution: $0.001 \mu\text{m}$ (squares), $0.01 \mu\text{m}$ (circles), and $0.03 \mu\text{m}$ (triangles).

moved from the distribution, a global reduction of effective pressure may be expected (lesser gas confinement). Quantitatively, the new value expected at zero pressure is $P_{\text{eff}}(0) = 3D_3/v(\lambda_c + l)$, and the relative impact of the truncation rapidly increases as l/λ_c increases. The truncation also induces a change of the P_{eff} increase rate over the whole pressure range, related to the modification of the probability distribution. This effect depends on the lower bound values l , as shown in Fig.16 for three exponential distributions (here also, line styles vary with characteristic mfp values λ_c). For instance, detailed comparison of the results obtained with lower bounds $l = 0.01 \mu\text{m}$ (circles) and $l = 0.03 \mu\text{m}$ (triangles), with reference to those obtained with $l = 0.001 \mu\text{m}$ (squares) in Fig.16 yields the following results: 1/ The relative P_{eff} changes computed at fixed pressure, for $P_3 = 4.8$ bars, amount to 30%, 10% and 0.5% for $\lambda_c = 0.05, 0.2,$ and $5 \mu\text{m}$ (respectively) with lower bound $l = 0.01 \mu\text{m}$. They drop to 14%, 4% and 0.2% for $\lambda_c = 0.05, 0.2,$ and $5 \mu\text{m}$ (respectively) with lower bound $l = 0.03 \mu\text{m}$. 2/ These P_{eff} changes decrease slowly, but steadily, as the gas pressure increases. From $P_3 = 1$ mbar to $P_3 = 10$ bars, the exhibited variation is equal to 27% with lower bound $l = 0.01 \mu\text{m}$, and drops to 14% with lower bound $l = 0.03 \mu\text{m}$, for the three λ_c values.

The distribution may also be truncated at large mfp's to probe the sensitivity of the diffusion coefficient to such a limit. The influence of the upper bound L re-

mains extremely limited due to the exponentially vanishing statistical weight of the large aerogel mfp's, as long as the selected L value exceeds that of the characteristic mfp λ_c . Conversely, it is important for upper bounds L comparable to λ_c . The effective pressure at zero gas pressure depends, quite naturally, on the exponential factor $r = \exp(-L/\lambda_c)$, and it is expected to vary as $P_{\text{eff}}(0) = (3D_3/v\lambda_c) \times [1 + r \ln(r) / (1 - r)]^{-1}$. But P_{eff} changes must noticeably vary with gas pressure, being much larger at low pressures (restriction of atomic diffusive motion over large length scales has been lifted) than at high pressures (atom-atom scattering already sets a small mfp limit). In Fig.17, dotted lines show, for instance, the results obtained for truncated exponential distributions with $\lambda_c = 0.5 \mu\text{m}$, and comparable upper mfp bounds L . Symbols are used to specify

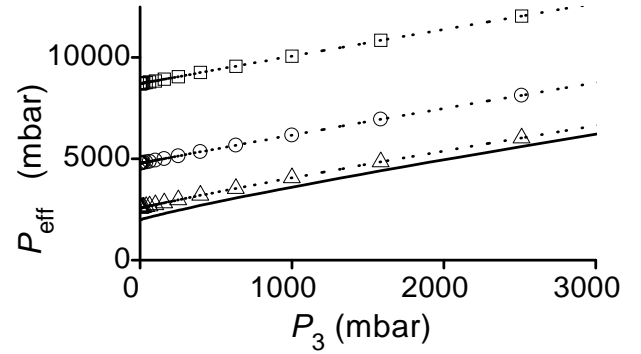


FIG. 17: Pressure dependence of P_{eff} for an exponential mfp distribution, with (broken lines) or without (solid line) truncation at large mfp's. The characteristic mfp of the distribution is $\lambda_c = 0.2 \mu\text{m}$. Data are computed for three upper bound L values: $0.1 \mu\text{m}$ (squares), $0.2 \mu\text{m}$ (circles), and $0.5 \mu\text{m}$ (triangles).

the selected L values, that vary from 0.1 to $0.5 \mu\text{m}$ (see caption). The $P_3 = 1$ mbar data differ from the zero pressure expected values $P_{\text{eff}}(0)$ by less than 0.2%, for the three L bounds. With reference to the unbounded distribution data (Fig.17, solid line), the P_{eff} increases due to the truncation vary from 4.35 (respectively: 2.39, and 1.29) at $P_3 = 1$ mbar, to 1.48 (respectively: 1.19, and 1.04) at $P_3 = 10$ bars, for $L = 0.1 \mu\text{m}$ (respectively: $L = 0.2 \mu\text{m}$, and $L = 0.5 \mu\text{m}$).

With or without truncation, exponential mfp distributions fail to provide effective diffusion coefficients that behave like the experimental ones.

In summary, for the three types of mfp distributions presented here, the computed pressure dependences exhibit features that do not correspond to the observed ones. A satisfactory description of the experimental diffusion data can only be obtained with the phenomenological power-law distributions introduced and characterized in the related article (Section V-B).

-
- [1] J. Fricke and T. Tillotson, *Thin Solid Films* **297**, 212 (1997).
- [2] D. W. Schaefer and K.D. Keefer, *Phys. Rev. Lett.* **56**, 2199 (1986).
- [3] J. Fricke, *Sci. Am.* **258**, 68 (1988).
- [4] A.C. Pierre and G.M. Pajonk, *Chem. Rev.* **102**, 4243 (2002).
- [5] Yu. K. Akimov, *Instrum. Exp.Tech. (USSR)* **46**, 287 (2003).
- [6] F. Ferri, B.J. Frisken, D.S. Cannell, and P. Wiltzius, *Phys. Rev. Lett.* **67**, 3626 (1991).
- [7] D. W. Schaefer, *Rev. Phys. Appl.* **50**, C4-121 (1989).
- [8] R. Vacher, T. Woignier, J. Pelous, and E. Courtens, *Phys. Rev. B* **37**, 6500 (1988).
- [9] B. J. Frisken, F. Ferri, and D. S. Cannell, *Phys. Rev. Lett.* **66**, 2754 (1991).
- [10] J. D. Reppy, *J. Low Temp. Phys.* **87**, 205 (1992).
- [11] A. P. Y. Wong, S. B. Kim, W. I. Goldberg, and M. H. W. Chan, *Phys. Rev. Lett.* **70**, 954 (1993).
- [12] J. V. Porto and J. M. Parpia, *Phys. Rev. B* **59**, 14583 (1999).
- [13] M.H.W. Chan, *Czech. J. Phys.* **46-S6**, 2915 (1996).
- [14] G. Lawes, S. C. Kingsley, N. Mulders, and J. M. Parpia, *Phys. Rev. Lett* **84**, 4148 (2000).
- [15] R. Hänninen and E. V. Thuneberg, *Phys. Rev. B* **67**, 214507 (2003).
- [16] J. Joon, D. Sergatskov, J. Mia, N. Mulders, and M. H. W. Chan, *Phys. Rev. Lett.* **80**, 1461 (1998).
- [17] J. V. Porto and J.M. Parpia, *Czech. J. Phys.* **46-S6**, 2981 (1996).
- [18] A. Singsaas and G. Ahlers, *Phys. Rev. B* **30**, 5103 (1984).
- [19] A. Boukenter, D. Champagnon, J. Dumas, E. Duval, J. F. Quinson, J. L. Rousset, J. Serughetti, S. Etienne, and C. Mai, *Rev. Phys. Appl.* **24**, C4-133 (1989).
- [20] A. Hasmy, E. Anglet, M. Foret, J. Pelous, and R. Jullien, *Phys. Rev. B* **50**, 6006 (1994).
- [21] C. Vasquez R., R. Paredes V., A. Hasmy, and R. Jullien, *Phys. Rev. Lett.* **90**, 170602 (2003).
- [22] S. Putselyk, G. Eska, S. Abe, and K. Matsumoto, *Physica B* **329**, 309 (2003).
- [23] G. W. Scherer, *Adv. Colloid Interface Sci.* **76-77**, 321 (1998).
- [24] P.P. Mitra, *Physica A* **241**, 122 (1997).
- [25] P.T. Callaghan, *Principles of Nuclear Magnetic Resonance Microscopy*, Oxford University Press, NY (1995).
- [26] R.K. Mazitov, P. Diehl and R. Seydoux, *Chem. Phys. Lett.* **201**, 543 (1993).
- [27] R. Seydoux and P. Diehl, *J. Magn. Reson. Ser. A* **119**, 76 (1996).
- [28] M.J. Lizak, M. S. Conradi, and C.G.Frey, *J. Magn. Reson.* **95**, 548 (1991).
- [29] D. Raftery, H. Long, T. Meersmann, P. J. Grandinetti, L. Reven, and A. Pines, *Phys. Rev. Lett.* **66**, 584 (1991).
- [30] Y.-Q. Song, H. C. Gaede, T. Pietrass, G. A. Barrall, G. C. Chingas, M. R. Ayers, and A. Pines, *J. Mag Reson.. A* **115**, 127 (1995).
- [31] B. Saam, N. Drukker, and W. Happer, *Chem. Phys. Lett.* **263**, 481 (1996).
- [32] C.H. Tseng, G.P. Wong, V.R. Pomeroy, R.W. Mair, D.P. Hinton, D. Hoffman, R.E. Stoner, F.W. Hersman, D.G. Cory, and R.L. Walsworth, *Phys. Rev. Lett.* **81**, 3785 (1998).
- [33] M. Salerno, T. A. Altes, J. P. Mugler III, M. Nakatsu, H. Hatabu, and E. E. de Lange, *Eur. J. Radiology* **40**, 33 (2001).
- [34] E. J. R. van Beek, J. M. Wild, H.-U. Kauczor, W. Schreiber, J. P. Mugler III, and E. E. de Lange, *J. Magn. Reson. Imaging* **20**, 540 (2004).
- [35] E. Durand, G. Guillot, L. Darrasse, G. Tastevin, P.-J. Nacher, A. Vignaud, D. Vatollo, and J. Bittoun, *Magn. Reson. Med.* **47**, 75 (2002).
- [36] C. P. Bidinosti, J. Choukeife, P.-J. Nacher, and G. Tastevin, *J. Magn. Reson.* **162**, 122 (2003). A slightly inaccurate numerical prefactor has been given for ^3He in Table B.1. The temperature fit in the 200-400K range actually gives $\mathcal{D}_3 = 1.967 \times (T/300)^{1.71} \text{ atm} \times \text{cm}^2/\text{s}$. The diffusion coefficient for isotopic mixtures must be accordingly modified: $\mathcal{D}_{3-4} = 1.840 \times (T/300)^{1.71} \text{ atm} \times \text{cm}^2/\text{s}$. Also, consequently, in G. Tastevin, *et al*, *Physica B* **329-333**, 303 (2003), the correct values of the diffusion coefficients at 1 mbar and 293 K are $D_3^1 = 1914 \text{ cm}^2/\text{s}$ for ^3He , and $D_{N_2}^1 = 790 \text{ cm}^2/\text{s}$ for ^3He in N_2 (a 1% and 1.4% change, respectively, due to the combined former errors in \mathcal{D}_3 and pressure units).
- [37] G. Tastevin, P.J. Nacher, and G. Guillot, *Physica B* **284-288**, 291 (2000).
- [38] G. Tastevin, P.J. Nacher, and G. Guillot, *J. Low Temp. Phys.* **121**, 773 (2000).
- [39] G. Guillot, P.J. Nacher, and G. Tastevin, *Magn. Reson. Imaging* **19**, 391 (2001).
- [40] D. Candela and N. Kalechofsky, *J. Low Temp. Phys.* **113**, 351 (1998).
- [41] T. M. Tillotson, L. W. Hrubesh, and I. M. Thomas, *Mater. Reson. Soc. Symp. Proc.* **121**, 685 (1988).
- [42] J.V. Porto, *PhD thesis: "Superfluid ^3He in aerogel"*, Cornell University, 1997 (unpublished).
- [43] T. M. Haard, G. Gervais, R. Nomura, and W. P. Halperin, *Physica B* **329-333**, 289 (2003).
- [44] K. J. McElroy, K. S. White, H. M. Bolzer, and C. M. Gould, *Physica B* **329-333**, 318 (2003).
- [45] Poly-(methyl methacrylate) is a common clear plastic, marketed under Plexiglas (Rohm and Haas, Philadelphia PA, USA) or Lucite (Lucite International, Southampton, UK) brand names, for instance.
- [46] S. Meiboom and D. Gill, *Rev. Sci. Instrum.* **29**, 688 (1958).
- [47] P.-J. Nacher, G. Tastevin, X. Maitre, X. Dollat, B. Lemaire and J. Olejnik., *Eur. Radiol.* **9**, B18 (1999).
- [48] B. Saam, W. Happer and H. Middleton, *Phys. Rev. A* **52** 862 (1995).
- [49] J. Choukeife, X. Maitre, P.J. Nacher, and G. Tastevin, *Magn. Reson. Mater. Phys. Biol. and Med.* **15-S1**, 201 (2002).
- [50] B. Pütz, D. Barsky, and K. Schulten, *J. Magn. Reson.* **97**, 27 (1992).
- [51] P. T. Callaghan, A. Coy, L.C. Forde, and C.J. Rofe, *J. Magn. Reson., Ser. A* **101**, 347 (1993).
- [52] Y.-Q. Song, B.M. Goodson, B. Sheridan, T.M. de Swiet, and A. Pines, *J. Chem. Phys.* **108**, 6233 (1998).
- [53] R.C. Wayne and R.M. Cotts, *Phys. Rev.* **151**, 264 (1966).

- [54] T.M. de Swiet and P. N. Sen, *J. Chem. Phys.* **100**, 5597 (1994);
- [55] M.D. Hürlimann, K.G. Kelmer, Y.M. de Swiet, P.N. Sen, and C.H. Sotak, *J. Magn. Reson. Ser. A* **113**, 260 (1995)
- [56] M.E. Hayden, G. Archibald, K.M. Gilbert, and C. Lei, *J. Magn. Reson.* **169**, 313 (2004).
- [57] N.R. Newbury, A.S. Burton, G.D. Cates, W. Happer, and H. Middleton, *Phys. Rev. A* **48**, 4411 (1993).
- [58] W.A. Fitzsimmons, L.L. Tankersley, and G.K. Walters, *Phys. Rev.* **179**, 156 (1969).
- [59] W. Heil, H. Humblot, E. Otten, M. Schaffer, R. Surkau, and M. Leduc, *Phys. Lett. A* **201**, 337 (1995).
- [60] R.E. Jacob, B. Driehyus, and B. Saam, *Chem. Phys. Lett.* **370**, 261 (2003).
- [61] P.-J. Nacher and G. Tastevin, to be published.
- [62] T.R. Gentile, D.R. Rich, A.K. Thompson, W.M. Snow, and G.L. Jones, *J. Res. Natl. Inst. Stand. Technol.* **106**, 709 (2001).
- [63] W. Heil, J. Dreyer, D. Hofmann, H. Humblot, E. Lelievre-Berna, and F. Tasset, *Physica B* **267-268**, 328 (1999).
- [64] W. Heil, private communication; J. Schmiedeskamp *et al*, to be published.
- [65] R.E. Jacob, S.W. Morgan, B. Saam, and J.C. Leawoods, *Phys. Rev. Lett.* **87**, 143004 (2003).
- [66] R.E. Jacob, J. Teter, B. Saam, W.C. Chen, and T.R. Gentile, *Phys. Rev. A* **69**, 021401(R) (2004).
- [67] E. Stejskal and J. Tanner, *J. Chem. Phys.* **42**, 288(1965).
- [68] L. van der Weerd, F.J. Vergeldt, P.A. de Jager, and H. Van As, *Magn. Reson. Imaging* **18**, 1151 (2000).
- [69] Our computed \mathcal{D}_3 value [36] has been confirmed by a very recent precise NMR measurement with hyperpolarized gas, reported in Ref. [56]: $0.140(6) \text{ m}^2/\text{s}$ for pure ^3He gas at 296 K and 1.00 torr, in perfect agreement with $D_{\text{gas}} = 1.967 \times (296/300)^{1.71} \times 760 = 0.1461 \text{ m}^2/\text{s}$.
- [70] L. Darrasse, G. Guillot, P.-J. Nacher, and G. Tastevin, *C.R. Acad. Sci. Paris* **324**, 691 (1997).
- [71] The relevant mfp λ is computed from the diffusion coefficient: $D = v\lambda/3$. In the particular case of self-diffusion in a single gas, λ is twice the usual collisional mfp, as defined from molecular diameter or obtained from other transport coefficients such as viscosity or heat conduction (see, e.g.: J. Jeans, *An introduction to the kinetic theory of gases*, Cambridge University Press, 1948, pp. 207-210). In pure ^3He , λ is thus equal to $400 \mu\text{m}$ at 1 mbar for free gas diffusion at 293 K .
- [72] See EPAS Document E-JCPA6-123-034528 for plots and discussion of the pressure dependence obtained for D_{eff} when aerogel-free spaces are taken into account, or when other types of mfp distributions in aerogel are used. This document can be reached via a direct link in the online article's HTML reference section or via the EPAPS homepage (<http://www.aip.org/pubservs/epaps.html>).
- [73] In the literature, experiments similar to ours would sometimes be presented as 'self-diffusion' measurements (here, performed in a confined geometry), because atoms just move with thermal velocities. They are, hereby, explicitly opposed to the so-called gas 'diffusion' measurements where atoms diffuse in response to a pressure gradient, that is applied across the porous sample. In this very common type of measurements, an additional drift velocity is imposed to the atoms by the pressure-driven motion.
- [74] D. M. Gregory, R. E. Gerald II, and R. E. Botto, *J. Magn. Reson.* **131**, 327 (1998).
- [75] D. M. Gregory and R. E. Botto, *Appl. Spectrosc.* **57**, 245 (2003).
- [76] D. P. Gallegos, D. M. Smith, and C. J. Brinker, *J. Colloid Interface Sci.* **124**, 186 (1988).
- [77] W. Behr, A. Haase, G. Reichenauer, and J. Fricke, *J. Non-Cryst. Solids* **225**, 91 (1998).
- [78] C. Stumpf, K. von Gaessler, G. Reichenauer, and J. Fricke, *J. Non-Cryst. Solids* **145**, 180 (1992).
- [79] S. Satoh, I. Matsuyama, and K. Susa, *J. Non-Cryst. Solids* **190**, 206 (1995).
- [80] G. Reichenauer, C. Stumpf, and J. Fricke, *J. Non-Cryst. Solids* **186**, 334 (1995).
- [81] B. Hosticka, P. M. Norris, J. S. Brenizer, and C. E. Daitch, *J. Non-Cryst. Solids* **225**, 293 (1998).
- [82] I. Beurroies, D. Bourret, R. Sempéré, L. Duffours, and J. Phalippou, *J. Non-Cryst. Solids* **186**, 328 (1995).
- [83] A. Hasmy, I. Beurroies, D. Bourret, and R. Jullien, *Europhys. Lett.* **29**, 567 (1995).
- [84] P. Levitz, *J. Phys. Chem.* **97**, 3813 (1993).
- [85] A. Hasmy, N. Olivi-Tran, and R. Jullien, *J. Phys.: Condens. Matter* **10**, 4947 (1998).
- [86] A. Hasmy and N. Olivi-Tran, *Phys. Rev. E* **59**, 3012 (1999).
- [87] C. P. Bidinosti, J. Choukeife, G. Tastevin, A. Vignaud, and P.-J. Nacher, *Magn. Reson. Mater. Phys. Biol. and Med. (MAGMA)* **16**, 255 (2004).
- [88] S. FICHELE, N. Woodhouse, A.J. Swift, Z. Said, M.N.J. Paley, L. Kasuboski, G.H. Mills, E.J.R. van Beek, and J.M. Wild, *J. Magn. Reson. Imaging* **20**, 331 (2004).
- [89] M. Salerno, E.E. de Lange, T.A. Altes, J.D. Truwit, J.R. Brookman, and J.P. Mugler III, *Radiology* **222**, 252 (2002).
- [90] B.T. Saam, D.A. Yablonskiy, V.D. Kodibagkar, J.C. Leawoods, D.S. Gierada, J.C. Cooper, S.S. Lefreak, and M.S. Conradi, *Magn. Reson. Med.* **44**, 174 (2000).
- [91] A.J. Swift, J.M. Wild, S. FICHELE, N. Woodhouse, R.A. Lawson, M.N.J. Paley, and E.J.R. van Beek, *Eur. J. Radiol.* **54**, 352 (2005).
- [92] R.H. Acosta, P. Blümmler, S. Han, S. Appelt, F.W. Häsing, J. Schmiedeskamp, W. Heil, and H.W. Spiess, *Magn. Reson. Imaging* **22**, 1077 (2004).
- [93] J. R. Owers-Bradley, M.S. FICHELE, A. Bennattayalah, C.J. Smith McGloin, R.W. Bowtell, P.S. Morgan, and A.R. Moody, *J. Magn. Reson. Imaging* **17**, 142 (2003).
- [94] J.C. Woods, D.A. Yablonskiy, K. Chino, T.S.Q. Tanoli, J.C. Cooper, and M.S. Conradi, *Magn. Reson. Med.* **51**, 1002 (2004).
- [95] X.J. Chen, H.E. Möller, M.S. Chawla, G.P. Cofer, B. Driehyus, L.W. Hedlund, and G.A. Johnson, *Magn. Reson. Med.* **42**, 721 (1999).
- [96] D.A. Yablonskiy, A.L. Sukstanskii, J.C. Leawoods, D.S. Gierada, G.L. Bretthorst, S.S. Lefrak, J.C. Cooper, and M.S. Conradi, *Proc. Natl. Acad. Sc.* **99**, 3111 (2002).
- [97] S. FICHELE, M.N.J. Paley, N. Woodhouse, P.D. Griffiths, E.J.R. van Beek, and J.M. Wild, *J Magn Reson.* **167**, 1 (2004); *Magn. Reson. Med.* **52**, 917 (2004).
- [98] D.D. McGregor, *Phys. Rev. A* **41**, 2361 (1990).
- [99] R.W. Mair, G.P. Wong, D. Hoffmann, M.D. Hürlimann, S. Patz, L.M. Schwartz, and R.L. Walsworth, *Phys. Rev. Lett.* **83**, 3324 (1999).

- [100] R.W. Mair, M.S. Rosen, R. Wang, D.G. Cory, and R.L. Walsworth, *Magn. Reson. Chem.* **40**, S29 (2002).
- [101] R. Wang, R.W. Mair, M.S. Rosen, D.G. Cory, and R.L. Walsworth, *Phys. Rev. E* **70**, 026312 (2004).